

Real-Time Regularized Ultrasound Elastography

Hassan Rivaz, Emad M. Boctor, Michael A. Choti and Gregory D. Hager

Abstract—This paper introduces two real-time elastography techniques based on analytic minimization (AM) of regularized cost functions. The first method (1D AM) produces axial strain and integer lateral displacement, while the second method (2D AM) produces both axial and lateral strains. The cost functions incorporate similarity of RF data intensity and displacement continuity, making both AM methods robust to small decorrelations present throughout the image. We also exploit techniques from robust statistics to make the methods resistant to large local decorrelations. We further introduce Kalman filtering for calculating the strain field from the displacement field given by the AM methods. Simulation and phantom experiments show that both methods generate strain images with high SNR, CNR and resolution. Both methods work for strains as high as 10% and run in real-time. We also present *in-vivo* patient trials of ablation monitoring. An implementation of the 2D AM method as well as phantom and clinical RF-data can be downloaded from http://www.cs.jhu.edu/~rivaz/Ultrasound_Elastography/.

Index Terms—Real-time ultrasound elastography, 2D strain, regularization, robust estimation, Kalman filter, RF ablation.

I. INTRODUCTION

ELASTOGRAPHY involves imaging the mechanical properties of tissue and has numerous clinical applications. Among many variations of ultrasound elastography [1], [2], [3], [4], our work focuses on real-time static elastography, a well-known technique that applies quasi-static compression of tissue and simultaneously images it with ultrasound. Within many techniques proposed for static elastography, we focus on freehand palpation elasticity imaging which involves deforming the tissue by simply pressing the ultrasound probe against it. It requires no extra hardware, provides ease of use and has attracted increasing interest in recent years [5], [6], [7], [8], [9], [10]. Real-time elastography is of key importance in many diagnosis applications [11], [6], [12], [8], [13] and in guidance/monitoring of surgical operations [14], [15], [16].

Global and local decorrelation between the pre- and post-compression ultrasound images compromises the quality of the elasticity images. The main sources of global decorrelation in freehand palpation elastography are change of speckle appearance due to scatterer motion and out-of-plane motion of the probe (axial, lateral and out-of-plane directions are specified in Figure 1). Examples of local decorrelation are: (1) a decrease in the ultrasonic signal to noise ratio with depth, (2) low correlation close to arteries due to complex motion and

inside blood vessels due to blood motion, (3) extremely low correlation in lesions that contain liquid due to the incoherent fluid motion [17], [8], and (4) out-of-plane motion of movable structures within the image [17].

Most elastography techniques estimate local displacements of tissue based on amplitude correlation [18], [2] or phase correlation of the radio-frequency (RF) echoes [19], [20], [21]. Assuming a stationary signal model for the RF data, the use of large correlation windows helps to reduce jitter errors (variance) for all motion field estimation techniques studied in [18], [22]. This is intuitive as larger windows contain more information. However, in practice RF data is not stationary and, for large deformations, the decorrelation increases with window size. Therefore, in addition to reducing the spatial resolution [23], larger windows result in significant signal decorrelation [24], [23], [18]. Coarse-to-fine hierarchical search is used in [23] to combine the accuracy of large windows with the good spatial resolution of small window. However, the issue of signal decorrelation within the window remains unresolved in this approach and can cause the highest level of the hierarchical search to fail.

All of the aforementioned methods either do not calculate the lateral displacement or they just calculate an approximate integer lateral displacement. A 2D displacement field is required to calculate the thermal expansion, lateral and shear strain fields [25] (i.e. reconstruct the strain tensor), Poisson's ratio and Young's modulus [26], [27]. The axial resolutions of ultrasound is determined by the pulse length, and the lateral resolutions is dictated by the center frequency of the excitation and the transducer pitch. Therefore, the lateral resolution is of order of magnitude lower than axial resolution. As a result, few 2D elastography techniques have been proposed to date. Initially, 2D motion estimation started in the field of blood flow estimation using speckle tracking [28]. Designed for blood flow estimation, these techniques are not immediately suitable for elastography which involves tissue deformation.

Attaching a coordinate system to the ultrasound probe as in Figure 1, z , x and y in the ultrasound image are generally defined as axial, lateral and elevational directions. Assume that the applied compression to the tissue is the Z direction, and attach a coordinate system X, Y, Z to the applied force. Letting d_Z and d_N be the displacements in the Z and N directions where $N \perp Z$, axial and transverse strains are $\partial d_Z / \partial Z$ and $\partial d_N / \partial N$. In most experimental setups (including freehand palpation elastography), z and Z are parallel and N will be either lateral or out-of-plane, and therefore d_N cannot be estimated accurately. To calculate an accurate transverse strain, Z and z are perpendicular in [29] by applying the compression force perpendicular to the ultrasound imaging axis. Therefore, transverse strain is in the z direction of the ultrasound probe and hence can be measured with high accuracy. However,

Manuscript received February 9, 2010; revised March 10, 2010.

Copyright (c) 2010 IEEE. Personal use of this material is permitted. However, permission to use this material for any other purposes must be obtained from the IEEE by sending a request to pubs-permissions@ieee.org. H. Rivaz is supported by the DoD Predoctoral Traineeship Award and by the Advanced Simulation Fellowship from the Link Foundation.

H. Rivaz, E. Boctor and G. Hager are with the Engineering Research Center for Computer Integrated Surgery, Johns Hopkins University.

M. Choti is with the Department of Surgery, Johns Hopkins Medicine.

such an experimental setup is not possible in many medical applications. Beam steering has been used to solve this issue [30]. In freehand palpation elastography, beam steering causes z and Z to be unparallel, so that a component of the d_X is in the z direction. The steering angle determines the angle between z and Z . Unfortunately, large steering angles are required to obtain accurate estimates of lateral strain, which is possible in phased arrays and not in linear arrays.

Lateral strain¹ estimation is obtained in [31] by iteratively calculating axial strain, companding RF data and interpolating in the lateral direction. In another work [32], tissue deformation is modeled by locally affine transformations to obtain both lateral and axial strains. Change of speckle appearance is taken into account by proposing a Lagrangian speckle model [33]. Although they provide high quality lateral strain, these techniques are computationally expensive and are not suitable for real-time implementation.

Axial strain is used in [34] to enhance the quality of lateral displacement estimation. Tissue is assumed to be incompressible and isotropic and therefore axial, lateral and out-of-plane strains should add to zero. However, many tissues cannot be considered incompressible. In fact, some research has even focused on imaging the ratio of the axial and lateral strain (i.e. the Poisson's ratio ν) [31].

While most previously mentioned methods use tissue motion continuity to confine the search range for the neighboring windows, the displacement of each window is calculated independently and hence is sensitive to signal decorrelation. Since data alone can be insufficient due to signal decorrelation, Pellot-Barakat et al. [35] proposed minimizing a regularized energy function that combines constraints of conservation of echo amplitude and displacement continuity. In another work [36], both signal shift and scale are found through minimization of a regularized cost function. The computation time of these methods is reported to be few minutes and therefore are not immediately suitable for real time elastography. In [37], [38], few phase-based methods are regularized and strain and elasticity modulus images are obtained. The regularization term is the Laplacian (second derivative) of the motion field and is spatially variant based on the peak-value of the correlation coefficient. The regularization makes the method significantly more robust to signal decorrelation. However, it is still prone to decorrelation within each window especially for large strain rates. In a recent work [39], a displacement field is first calculated by minimizing phase differences in correlation windows [21]. The strain image is then estimated from the displacement field by optimizing a regularized cost function. The regularization assures smooth strain image calculation from the noisy displacement estimates.

We have proposed optimizing a recursive regularized cost function using Dynamic Programming (DP) [40]. DP is used to speed the optimization procedure, but it only gives integer displacements. Subsample displacement estimation is possible [40], but it is computationally expensive, particularly if subsample accuracy is needed in both axial and lateral

directions. Therefore, only axial subsample displacement is calculated [40]. In addition, a fixed regularization weight is applied throughout the image. To prevent regions with high local decorrelation from introducing errors in the displacement estimation one should use large weights for the regularization term, resulting in over-smoothing.

In this paper, we present two novel real-time elastography methods based on analytic minimization (AM) of cost functions that incorporate similarity of echo amplitudes and displacement continuity. Similar to DP, the first method gives subsample axial and integer lateral displacements. The second method gives subsample 2D displacement fields and 2D strain fields. The size of both displacement and strain fields is the same size as the RF-data (i.e. the methods are not window based and the displacement and strain fields are calculated for all individual samples of RF-data). We introduce a novel regularization term and demonstrate that it minimizes displacement underestimation caused by smoothness constraint. We also introduce the use of robust statistics implemented via iterated reweighted least squares (IRLS) to treat uncorrelated ultrasound data as outliers. Finally, for the first time to the best of our knowledge we introduce the use of Kalman filtering [41] for calculating strain image from the displacement field. Simulation and experimental results are provided for quantitative validation. The paper concludes with a clinical pilot study utilizing this system for monitoring thermal ablation in patients with liver tumors.

II. METHODS

Assume that the tissue undergoes a deformation and let I_1 and I_2 be two images acquired from the tissue before and after the deformation. Letting I_1 and I_2 be of size $m \times n$ (Figure 1), our goal is to find two matrices A and L where the $(i, j)^{th}$ component of A ($a_{i,j}$) and L ($l_{i,j}$) are the axial and lateral motion of the pixel (i, j) of I_1 (we are not calculating the out-of-plane motion). The axial and lateral strains are easily calculated by spatially differentiating A in the axial direction (resulting in A_a) and L in the lateral direction (resulting in L_l). The shear strains (not calculated in this work) can also be easily calculated by spatially differentiating A in the lateral direction (resulting in A_l) or L in the axial direction (resulting in L_a).

In this section, we first give a brief overview of a previous work (DP) that calculates integer values for A and L . We then propose 1D Analytic Minimization (AM) as a method that takes the integer displacement field from DP and refines the axial displacement component. We then introduce 2D Analytic Minimization (AM) that takes the integer displacement of a single RF-line from DP and gives the subsample axial and lateral displacement fields for the entire image. We conclude this section by presenting a technique for calculating smooth strain field from the displacement field using Kalman filtering.

A. Dynamic Programming (DP)

In order to present the general DP formulation, we consider a single column j (an RF-line) in I_1 (the image before deformation) in Figure 1. Let m and n be the length of the

¹We hereafter assume the applied force is in the z direction (i.e. Z and z are parallel) and therefore we use the term lateral strain instead of the term transverse strain.

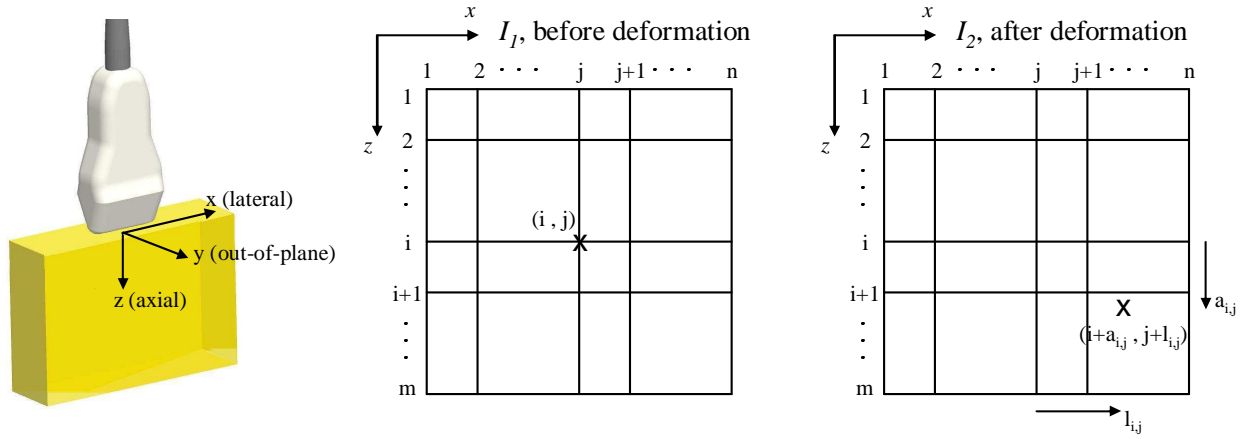


Fig. 1. Axial, lateral and out-of-plane directions. The coordinate system is attached to the ultrasound probe. The sample (i, j) marked by x moved by $(a_{i,j}, l_{i,j})$. $a_{i,j}$ and $l_{i,j}$ are respectively axial and lateral displacements and initially are integer in DP.

RF-lines and the number of RF-lines in the images (Figure 1). Let a_i and l_i denote the axial and lateral displacements of the i^{th} sample of the RF-line in column j . In DP elastography [40], a regularized cost function is generated by adding the prior of displacement continuity (the regularization term) to an amplitude similarity term. The displacement continuity term for column j is

$$R_j(a_i, l_i, a_{i-1}, l_{i-1}) = \alpha_a (a_i - a_{i-1})^2 + \alpha_l (l_i - l_{i-1})^2 \quad (1)$$

which forces the displacements of the sample i (i.e. a_i and l_i) be similar to the displacements of the previous sample $i-1$ (i.e. a_{i-1} and l_{i-1}). α_a and α_l are axial and lateral regularization weights respectively. We write $R_j(a_i, l_i, a_{i-1}, l_{i-1})$ to indicate the dependency of a_i and l_i on j . The regularized cost function for column j is then generated as following

$$C_j(a_i, l_i, i) = [I_1(i, j) - I_2(i + a_i, j + l_i)]^2 + \min_{d_a, d_l} \left\{ \frac{C_j(d_a, d_l, i-1) + C_{j-1}(d_a, d_l, i)}{2} + R_j(a_i, l_i, d_a, d_l) \right\} \quad (2)$$

where d_a and d_l are temporary displacements in the axial and lateral directions that are varied to minimize the term in the bracket. After calculating C_j for $i = 2 \dots m$, C_j is minimized at $i = m$ giving a_m and l_m . The a_i and l_i values that have minimized the cost function at $i = m$ are then traced back to $i = 1$, giving integer a_i and l_i for all samples of j^{th} line. The process is performed for the next line $j+1$ until the displacement of the whole image is calculated. The 2D DP method gives integer axial and lateral displacement maps. In [40], we performed hierarchical search to obtain subsample axial displacement (the lateral displacement was not refined to subsample). DP is an efficient method for global optimization and has been used extensively in many applications in computer vision including solving for optimal deformable models [42]. In the next section, we propose an alternative method for calculating subsample axial displacement which is both faster and more robust than hierarchical DP.

B. 1D Analytic Minimization (AM)

Tissue deformations in ultrasound elastography are usually very small and therefore a subsample displacement estima-

tion is required. We now develop a method that analytically minimizes a regularized cost function and gives the refined displacement field following the work presented in [16]. We first consider a specialization of Equation 2 in which we only consider refining axial displacements to subsample level.

Having the integer displacements a_i and l_i from DP, it is desired to find Δa_i values such that $a_i + \Delta a_i$ gives the value of the displacement at the sample i for $i = 1 \dots m$ (l_i , a_i and Δa_i correspond to line j . Hereafter, wherever the displacements correspond to the j^{th} line, j is omitted to prevent notation clutter). Such Δa_i values will minimize the following regularized cost function

$$C_j(\Delta a_1, \dots, \Delta a_m) = \sum_{i=1}^m \left\{ [I_1(i, j) - I_2(i + a_i + \Delta a_i, j + l_i)]^2 + \alpha_a (a_i + \Delta a_i - a_{i-1} - \Delta a_{i-1})^2 + \alpha_l (a_i + \Delta a_i - a_{i,j-1} - \Delta a_{i,j-1})^2 \right\} \quad (3)$$

where $\alpha_a > 0$ and $\alpha_l > 0$ are tunable axial and lateral regularization weights and subscript $j-1$ refers to the previous RF-line (adjacent RF-line in the lateral direction). Substituting $I_2(i + d_i + \Delta d_i)$ with its first order Taylor expansion approximation around d_i , we have

$$C_j(\Delta a_1, \dots, \Delta a_m) = \sum_{i=1}^m \left\{ [I_1(i, j) - I_2(i + a_i, j + l_i) - I_2'(i + a_i, j + l_i) \Delta a_i]^2 + \alpha_a (a_i + \Delta a_i - a_{i-1} - \Delta a_{i-1})^2 + \alpha_l (a_i + \Delta a_i - a_{i,j-1} - \Delta a_{i,j-1})^2 \right\} \quad (4)$$

where I_2' is the derivative of the I_2 in the axial direction. The optimal Δa_i values occur when the partial derivative of C_j with respect to Δa_i is zero. Setting $\frac{\partial C_j}{\partial \Delta a_i} = 0$ for $i = 1 \dots m$ we have

$$(I_2'^2 + \alpha_a \mathbf{D} + \alpha_l \hat{\mathbf{I}}) \Delta \mathbf{a}_j = I_2' \mathbf{e} - (\alpha_a \mathbf{D} + \alpha_l \hat{\mathbf{I}}) \mathbf{a}_j + \alpha_l \mathbf{a}_{j-1}, \quad (5)$$

$$\mathbf{D} = \begin{bmatrix} 1 & -1 & 0 & 0 & \cdots & 0 \\ -1 & 2 & -1 & 0 & \cdots & 0 \\ 0 & -1 & 2 & -1 & \cdots & 0 \\ \vdots & & & & \ddots & \\ 0 & 0 & \cdots & 0 & -1 & 1 \end{bmatrix} \quad (6)$$

where $\mathbf{I}'_2 = \text{diag}(I'_2(1 + d_1, j + l_i) \cdots I'_2(m + d_m, j + l_i))$, $\Delta \mathbf{a}_j = [\Delta a_{1,j} \cdots \Delta a_{m,j}]^T$, $\mathbf{e} = [e_1 \cdots e_m]^T$, $e_i = I_1(i, j) - I_2(i + d_i, j + l_i)$, $\mathbf{a}_j = [a_{1,j} \cdots a_{m,j}]^T$, $\hat{\mathbf{I}}$ is the identity matrix and \mathbf{a}_{j-1} is the total displacement of the previous line (i.e. when the displacement of the $j-1^{\text{th}}$ line was being calculated, \mathbf{a}_{j-1} was updated with $\mathbf{a}_{j-1} + \Delta \mathbf{a}_{j-1}$). \mathbf{I}'_2 , \mathbf{D} and $\hat{\mathbf{I}}$ are matrices of size $m \times m$ and $\Delta \mathbf{a}$, \mathbf{e} and \mathbf{a} are vectors of size m .

Comparing 1D AM (as formulated in Equation 5) and 2D DP, they both optimize the same cost function. Therefore, they give the same displacement fields (up to the refinement level of the DP). In the next two subsections, we will further improve 1D AM.

1) *Biassing the Regularization:* The regularization term $\alpha_a(a_i + \Delta a_i - a_{i-1} - \Delta a_{i-1})^2$ penalizes the difference between $a_i + \Delta a_i$ and $a_{i-1} + \Delta a_{i-1}$, and therefore can result in underestimation of the displacement field. Such underestimation can be prevented by biasing the regularization by ϵ to $\alpha_a(a_i + \Delta a_i - a_{i-1} - \Delta a_{i-1} - \epsilon)^2$, where $\epsilon = (a_m - a_1)/(m-1)$ is the average displacement difference (i.e. average strain) between samples i and $i-1$. An accurate enough estimate of $d_m - d_1$ is known from the previous line. With the bias term, the R.H.S. of Equation 5 becomes $\mathbf{I}'_2 \mathbf{e} - (\alpha_a \mathbf{D} + \alpha_l \hat{\mathbf{I}}) \mathbf{a}_j + \alpha_l (\mathbf{a}_{j-1} + \Delta \mathbf{a}_{j-1}) + \mathbf{b}$ where the bias term is $\mathbf{b} = \alpha_a [-\epsilon \ 0 \cdots 0 \ \epsilon]^T$ (only the first and the last terms are nonzero) and all other terms are as before. In the other words, except for the first and the last equations in this system, all other $m-2$ equations are same as Equation 5.

Equation 5 can be solved for $\Delta \mathbf{a}_j$ in $4m$ operations since the coefficient matrix $\mathbf{I}'_2 + \alpha_a \mathbf{D} + \alpha_l \hat{\mathbf{I}}$ is tridiagonal. Utilizing its symmetry, the number of operations can be reduced to $2m$. The number of operations required for solving a system with a full coefficient matrix is more than $m^3/3$, significantly more than $2m$.

2) *Making Elastography Resistant to Outliers:* Even with pure axial compression, some regions of the image may move out of the imaging plane and decrease the decorrelation. In such parts the weight of the data term in the cost function should be reduced. The data from these parts can be regarded as outliers and therefore a robust estimation technique can limit their effect. Before deriving a robust estimator for $\Delta \mathbf{a}$, we rewrite Equation 4 as

$$C(\Delta \mathbf{a}) = \sum_{i=1}^m \rho(r_i) + R(\Delta \mathbf{a}) \quad (7)$$

where $r_i = I_1(i) - I_2(i + a_i) - I'_2(i + a_i) \Delta a_i$ is the residual, $\rho(r_i) = r_i^2$ and R is the regularization term. The M-estimate of $\Delta \mathbf{a}$ is $\Delta \hat{\mathbf{a}} = \arg \min_{\Delta \mathbf{a}} \{ \sum_{i=1}^m \rho(r_i) + R(\Delta \mathbf{a}) \}$ where $\rho(r_i)$ is a robust loss function [43]. The minimization is solved by setting $\frac{\partial C}{\partial \Delta a_i} = 0$:

$$\rho'(r_i) \frac{\partial r}{\partial \Delta a_i} + \frac{\partial R(\Delta \mathbf{a})}{\partial \Delta a_i} = 0 \quad (8)$$

A common next step [44] is to introduce a weight function w , where $w(r_i) \cdot r_i = \rho'(r_i)$. This leads to a process known as “iteratively reweighted least squares” (IRLS) [45], which alternates steps of calculating weights $w(r_i)$ for $r_i = 1 \cdots m$ using the current estimate of $\Delta \mathbf{a}$ and solving Equation 8 to estimate a new $\Delta \mathbf{a}$ with the weights fixed. Among many proposed shapes for $w(\cdot)$, we compared the performance of Huber [44], [43]

$$w(r_i) = \begin{cases} 1 & |r_i| < T \\ \frac{T}{|r_i|} & |r_i| > T \end{cases} \quad (9)$$

and Cauchy [45]

$$w(r_i) = \frac{1}{1 + (r_i/T)^2} \quad (10)$$

functions and discovered that the more strict Cauchy function (which decreases with inverse of the *square* of the residual) is more suitable in our application. To better discriminate outliers, we calculate the residuals r_i at linear interpolation of the integer sample displacements provided by DP. With the addition of the weight function, Equation 8 becomes

$$(\mathbf{w} \mathbf{I}'_2 + \alpha_a \mathbf{D} + \alpha_l \hat{\mathbf{I}}) \Delta \mathbf{a}_j = \mathbf{w} \mathbf{I}'_2 \mathbf{e} - (\alpha_a \mathbf{D} + \alpha_l \hat{\mathbf{I}}) \mathbf{a}_j + \alpha_l \mathbf{a}_{j-1} + \mathbf{b} \quad (11)$$

where $\mathbf{w} = \text{diag}(w(r_1) \cdots w(r_m))$. This equation will converge to a unique local minimum after few iterations [45]. The convergence speed however depends on the choice of T , which in this work is defined manually. Since the Taylor approximation gives a local quadratic approximation of the original non-quadratic cost function, the effect of higher orders terms increase if Δa_j is large. Assuming that DP gives the correct displacements, $\|\Delta a_j\|_\infty \leq \epsilon$ where $\|\cdot\|_\infty$ is the infinity norm and $\epsilon \leq 0.5$. In practice, however, $\epsilon \ll 0.5$ because the linear interpolation of the DP displacements (which is very close to the correct displacement) is used to calculate the residuals r_i . Therefore, a small value can be assigned to T in 1D AM provided that DP results are trusted.

The coefficient matrix $Q = \mathbf{w} \mathbf{I}'_2 + \alpha_a \mathbf{D} + \alpha_l \hat{\mathbf{I}}$ in Equation 11 is the Hessian of the cost function C whose minimum is sought. This matrix is strictly diagonally dominant (i.e. $|q_{ii}| > \sum_{j \neq i} |q_{ij}|$ for all i where q_{ij} is the i, j^{th} element of Q), symmetric and all diagonal entries are positive. Therefore, it is positive definite, which means that setting the gradient of C to zero results in the global minimum of C (not in a saddle point, a local maximum or a local minimum). All of the 1D AM results presented in this work are obtained with one iteration of the above equation.

1D AM takes the integer axial and lateral displacement fields from DP and gives refined axial displacement. It inherits the robustness of DP and adds more robustness when calculating the fine axial displacements via IRLS. However, there are redundant calculations in this method which are eliminated in 2D AM as described next.

C. 2D Analytic Minimization (AM)

In 2D AM, we modify Equation 2 to calculate subsample axial and lateral displacement fields *simultaneously*. The outline of our proposed algorithm is as follows

- 1) Calculate the integer axial and lateral displacements of one or more *seed* RF-lines (preferably in the middle of the image) using DP (Equation 2). Calculate the linear interpolation of the integer displacements as an initial subsample estimate.
- 2) Calculate subsample axial and lateral displacements of the seed RF-line using 2D AM, as explained below. Add the subsample axial and lateral displacements to the initial estimate to get the displacement of the seed line.
- 3) Propagate the solution to the right and left of the seed RF-line using the 2D AM method, taking the displacement of the previous line as the initial displacement estimate.

Benefits of 2D AM are two-fold. First it computes subsample displacements in both axial and lateral directions. Lateral strain contains important information from tissue structure that is not available from axial strain [31], [46], [47]. Second, it is only required to calculate the displacement of a single line using DP (the seed), eliminating the need to have the integer displacement map for the entire image. This is significant as in the 1D AM method, the initial step to calculate the 2D integer displacements using DP takes about **10** times more than the 1D AM.

Assume that initial displacement estimates in the axial direction, a_i , and in the lateral direction, l_i , are known for all $i = 1 \cdots m$ samples of an RF-line. Note that a_i and l_i are not integer; for the seed line they are the linear interpolation of the integer DP displacements and for the rest of the lines are the displacement of the previous line. It is desired to find Δa_i and Δl_i values such that the duple $(a_i + \Delta a_i, l_i + \Delta l_i)$ gives the axial and lateral displacements at the sample i . Such $(\Delta d_i, \Delta a_i)$ values will minimize the following regularized cost function

$$C_j(\Delta a_1, \dots, \Delta a_m, \Delta l_1, \dots, \Delta l_m) = \sum_{i=1}^m \{ [I_1(i, j) - I_2(i + a_i + \Delta a_i, j + l_i + \Delta l_i)]^2 + \alpha(a_i + \Delta a_i - a_{i-1} - \Delta a_{i-1})^2 + \beta_a(l_i + \Delta l_i - l_{i-1} - \Delta l_{i-1})^2 + \beta_l'(l_i + \Delta l_i - l_{i,j-1})^2 \} \quad (12)$$

where $I(i, j)$ is the i^{th} sample on the j^{th} RF-line. Since we perform the calculations for one RF-line at a time, we dropped the index j to simplify the notations: a_i , l_i , Δa_i and Δl_i are $a_{i,j}$, $l_{i,j}$, $\Delta a_{i,j}$ and $\Delta l_{i,j}$. $l_{i,j-1}$ is the lateral displacement of the previous RF-line (note that $l_{i,j-1}$ is the total lateral displacement of the previous line, i.e. when the displacement of the $j - 1^{\text{th}}$ line was being calculated, $l_{i,j-1}$ was updated with $l_{i,j-1} + \Delta l_{i,j-1}$). Since in the first iteration a_i and l_i (the initial displacement estimates) are in fact the displacements of the previous RF-line, for the first iteration we have $l_{i,j-1} = l_i$. This simplifies the last term in the R.H.S. to $\beta_l' \Delta l_i^2$. The regularization terms are α , β_a and β_l' : α determines how close the axial displacement of each sample should be to its neighbor on the top and β_a and β_l' determine how close lateral displacement of each sample should be to its neighbors on the top and left (or right if propagating to the left). If the displacement of the previous line is not accurate, it will affect the displacement of the next line through the last

term in the R.H.S. of Equation 12. Although its effect will decrease exponentially with j , it will propagate for few RF-lines. Therefore we set

$$\beta_l' = \frac{\beta_l}{1 + |r_{i,j-1}|} \quad (13)$$

to prevent such propagation where $r_{i,j-1}$ is the residual associated with the displacement of the i^{th} sample of the previous line. A large residual indicates that the displacement is not accurate and therefore its influence on the next line should be small, which is realized via the small weight β_l' . This is, in principle, similar to guiding the displacement estimation based on a data quality indicator [48]. The effect of the tunable parameters α , β_a and β_l is studied in the Results section. Writing the 2D Taylor expansion of the data term in Equation 12 around $(i + a_i, j + l_i)$:

$$I_2(i + a_i + \Delta a_i, j + l_i + \Delta l_i) \approx I_2(i + a_i, j + l_i) + \Delta a_i I'_{2,a} + \Delta l_i I'_{2,l} \quad (14)$$

where $I'_{2,a}$ and $I'_{2,l}$ are the derivatives of the I_2 at point $(i + a_i, j + l_i)$ in the axial and lateral directions respectively. Note that since the point $(i + a_i, j + l_i)$ is not on the grid (a_i and l_i are not integer), interpolation is required to calculate $I'_{2,a}$ and $I'_{2,l}$. We propose a method in Section II-C1 that eliminates the need for interpolation. The optimal $(\Delta a_i, \Delta l_i)$ values occur when the partial derivatives of C_j with respect to both Δa_i and Δl_i are zero. Setting $\frac{\partial C_j}{\partial \Delta a_i} = 0$ and $\frac{\partial C_j}{\partial \Delta l_i} = 0$ for $i = 1 \cdots m$ and stacking the $2m$ unknowns in $\Delta \mathbf{d} = [\Delta a_1 \Delta l_1 \Delta a_2 \Delta l_2 \cdots \Delta a_m \Delta l_m]^T$ and the $2m$ initial estimates in $\mathbf{d} = [a_1 \ l_1 \ a_2 \ l_2 \ \cdots \ a_m \ l_m]^T$ we have

$$(\mathcal{I}_2'^2 + \mathcal{D}_1 + \mathcal{D}_2)\Delta \mathbf{d} = \mathcal{I}_2' \boldsymbol{\epsilon} - \mathcal{D}_1 \mathbf{d}, \quad (15)$$

$$\mathcal{D}_1 = \begin{bmatrix} \alpha & 0 & -\alpha & 0 & 0 & 0 & \cdots & 0 \\ 0 & \beta_a & 0 & -\beta_a & 0 & 0 & \cdots & 0 \\ -\alpha & 0 & 2\alpha & 0 & -\alpha & 0 & \cdots & 0 \\ 0 & -\beta_a & 0 & 2\beta_a & 0 & -\beta_a & \cdots & 0 \\ 0 & 0 & -\alpha & 0 & 2\alpha & 0 & \cdots & 0 \\ \vdots & & & & & & \ddots & \\ 0 & 0 & 0 & \cdots & -\alpha & 0 & \alpha & 0 \\ 0 & 0 & 0 & \cdots & 0 & -\beta_a & 0 & \beta_a \end{bmatrix}$$

where $\mathcal{D}_2 = \text{diag}(0, \beta_l', 0, \beta_l', \dots, 0, \beta_l')$ is a diagonal matrix of size $2m \times 2m$, $\mathcal{I}_2'^2 = \text{diag}(\mathcal{I}'^2(1) \cdots \mathcal{I}'^2(m))$ is a symmetric tridiagonal matrix of size $2m \times 2m$ with

$$\mathcal{I}'^2(i) = \begin{bmatrix} I'_{2,a}{}^2 & I'_{2,a} I'_{2,l} \\ I'_{2,a} I'_{2,l} & I'_{2,l}{}^2 \end{bmatrix} \quad (16)$$

blocks on its diagonal entries where $I'_{2,a}$ and $I'_{2,l}$ are the derivatives of the I_2 at point $(i + a_i, j + l_i)$ in the axial and lateral directions,

$$\mathcal{I}_2' = \text{diag}(I'_{2,a}(1), I'_{2,l}(1), I'_{2,a}(2), I'_{2,l}(2) \cdots I'_{2,a}(m), I'_{2,l}(m)) \quad (17)$$

where $I'_{2,a}(i)$ and $I'_{2,l}(i)$ are calculated at point $(i + a_i, j + l_i)$, and $\boldsymbol{\epsilon} = [e_1 \ e_1 \ e_2 \ e_2 \ \cdots \ e_m]^T$, $e_i = I_1(i, j) - I_2(i + a_i, j + l_i)$.

We make four modifications to Equation 15: First, we take into account the attenuation of the ultrasound signal with

depth. As the signal gets weaker with depth, the first term in the R.H.S. of Equation 15 ($\mathcal{I}_2'\epsilon$) gets smaller. This results in increasing the share of the regularization term in the cost C_j and therefore over-smoothing the bottom of the image. The attenuation of the ultrasound signal [49] reflected from the depth d is $\zeta(d) = e^{-2\log(10)a_t f_0 d/20}$ where a_t is the frequency dependent attenuation coefficient of tissue and is equal to 0.63 dB/cm/MHz for fat [49], f_0 is the center frequency of the wave (in MHz) and d is in cm. Having the exponential attenuation equation, the attenuation level at sample i will be

$$\zeta_i = x^{-i}, \quad x = e^{\frac{1540 \times 10^2 a_t f_0 \log(10)}{20 f_s \times 10^6}}, \quad i = 1 \cdots m \quad (18)$$

where 1540×10^2 is the speed of sound in tissue (in cm/sec) and f_s is the sampling rate of the ultrasound system (in MHz). This is assuming that the TGC (time gain control) is turned off. Otherwise, the TGC values should be taken into account in this equation. Let the $2m \times 2m$ diagonal matrix \mathbf{Z} be $\mathbf{Z} = \text{diag}(\zeta_1, \zeta_1, \zeta_2, \zeta_2 \cdots \zeta_m, \zeta_m)$. To compensate for the attenuation, we multiply the \mathcal{D}_1 and \mathcal{D}_2 matrices in Equation 15 by \mathbf{Z} , and therefore reduce the regularization weight with depth. As we will show in Sections III and IV, the regularization weight can vary substantially with no performance degradation. Therefore approximate values of the speed of sound and attenuation coefficient will suffice. Second, we add a bias term in the regularization similar to the 1D case. Here we only bias the axial displacement since the difference between the lateral displacements of the points on a RF-line is very small, usually less than 4 RF-lines. Third, we exploit the fact that, because the tissue is in contact with the ultrasound probe, the axial displacement of the top of the image is zero relative to the probe (the lateral displacement of the top of the image is not zero as tissue might slip under the probe). Therefore, we enforce the axial displacement of the first sample to be zero by changing the first row of \mathcal{D}_1 , $\mathcal{I}_2'^2$ and \mathcal{I}_2' . Fourth, we make the displacement estimation robust via IRLS using the Cauchy function (Equation 10). Similar to 1D AM, T is selected manually. For the first (seed) RF-line, a small value can be selected for T if DP results are trusted. For the next lines, the value of $\Delta \mathbf{d}$ determines the accuracy of the Taylor expansion 14: for a small $\Delta \mathbf{d}$, the residuals of the inliers are small and therefore a small T can be chosen, while for a large $\Delta \mathbf{d}$ the inliers might give large residuals and therefore a large value for T is required. Since the tissue motion is mostly continuous, $\Delta \mathbf{d}$ mostly depends on the lateral sampling of the image (i.e. the number of A-line per cm). Therefore if many A-lines are given per cm of the image width, a small value of T will give the optimum results. Since the amplitude of signal is decreasing due to attenuation, we decrease the IRLS parameter T with depth by multiplying it with ζ_i at each sample i . With these modifications, Equation 15 becomes

$$(\mathcal{W}\mathcal{I}_2'^2 + \mathbf{Z}\mathcal{D}_1 + \mathbf{Z}\mathcal{D}_2)\Delta \mathbf{d} = \mathcal{W}\mathcal{I}_2'\epsilon - \mathbf{Z}\mathcal{D}_1\mathbf{d} + \mathbf{s} \quad (19)$$

where $\mathcal{W} = \text{diag}(0, w(r_1), w(r_2), w(r_2) \cdots w(r_m), w(r_m))$ (i.e. $\mathcal{W}_{2i,2i} = \mathcal{W}_{2i-1,2i-1} = w(r_i)$ for $i = 1 \cdots m$ except for $\mathcal{W}_{1,1} = 0$ which guarantees the displacement of the first sample to be zero) is the weight function determined by the residuals $r_i = I_1(i, j) - [I_2(i + d_i, j + a_i) + \Delta d_i I_{2,z}' + \Delta a_i I_{2,x}']$,

w is as before (Equation 10), the bias term \mathbf{s} is a vector of length $2m$ whose all elements are zero except the $2m - 1^{\text{th}}$ element: $s_{2m-1} = \alpha\epsilon$, and $\epsilon = (d_m - d_1)/(m - 1)$ is as before. Similar to Equation 11, the coefficient matrix $\mathcal{Q} = \mathcal{W}\mathcal{I}_2'^2 + \mathbf{Z}\mathcal{D}_1 + \mathbf{Z}\mathcal{D}_2$ is strictly diagonally dominant, symmetric and all the diagonal entries are positive. Therefore \mathcal{Q} is positive definite which means that solving Equation 19 results in the global minimum of the cost function C . The updated displacement field (axial and lateral) will be $\mathbf{d} + \Delta \mathbf{d}$.

Equation 19 can be solved for $\Delta \mathbf{d}$ in $9m$ operations since the coefficient matrix $\mathcal{W}\mathcal{I}_2'^2 + \mathbf{Z}\mathcal{D}_1 + \mathbf{Z}\mathcal{D}_2$ is pentadiagonal and symmetric. This number is again significantly less than $(2m)^3/3$, the number of operations required to solve a full system.

1) *Inverse Gradient Estimation*: With the subsample initial displacement field, the Taylor expansion should be written around off-grid points, which requires calculation of image gradient at these points (matrices $\mathcal{I}_2'^2$ and \mathcal{I}_2' in Equation 19). In Figure 2 (a), this is equivalent to calculating gradient of I_2 on the off-grid marks. There are two disadvantages associated with this: 1) it requires interpolation of the gradients, and 2) the image gradient should be recalculated after each iteration. As proposed by [44], [50], image gradient can be instead calculated at on-grid locations on image 1 in the following way.

Consider two problems: (1) to find the matches for grid points on I_1 having the initial off-grid estimates on I_2 , and (2) to find the matches for the off-grid points on I_2 having the initial grid estimates on I_1 . For both problems, I_2 values must be interpolated on the off-grid values. However, the second problem does not require interpolation of the image gradient since the Taylor expansion is written around grid points of I_1 (Figure 2 (b)). It is shown in [51] that the two techniques converge to the same results. Therefore, on one hand inverse gradient calculation is both faster and easier to implement, and on the other hand it causes no performance degradation. Exploiting this, Equation 19 becomes

$$(\mathcal{W}\mathcal{I}_1'^2 + \mathbf{Z}\mathcal{D}_1 + \mathbf{Z}\mathcal{D}_2)\Delta \mathbf{d} = \mathcal{W}\mathcal{I}_1'\epsilon - \mathbf{Z}\mathcal{D}_1\mathbf{d} + \mathbf{s} \quad (20)$$

where $\mathcal{I}_1'^2$ and \mathcal{I}_1' are now calculated on the grid points of image 1.

All the 2D AM results presented in this work are obtained using Equation 20. For the seed line where the initial estimate might be inaccurate, this equation is iterated multiple times (about 10 times). For all other lines this equation is iterated only once.

D. Strain Estimation Using Kalman Filter

Strain estimation requires spatial derivation of the displacement field. Since differentiation amplifies the signal noise, least squares regression techniques are commonly used to obtain the strain field. Adjacent RF-lines are usually processed independently in strain calculation. However, the strain value of each pixel is not independent from the strain value of its neighboring pixels. The only exception is the boundary of two tissue types with different mechanical properties where the

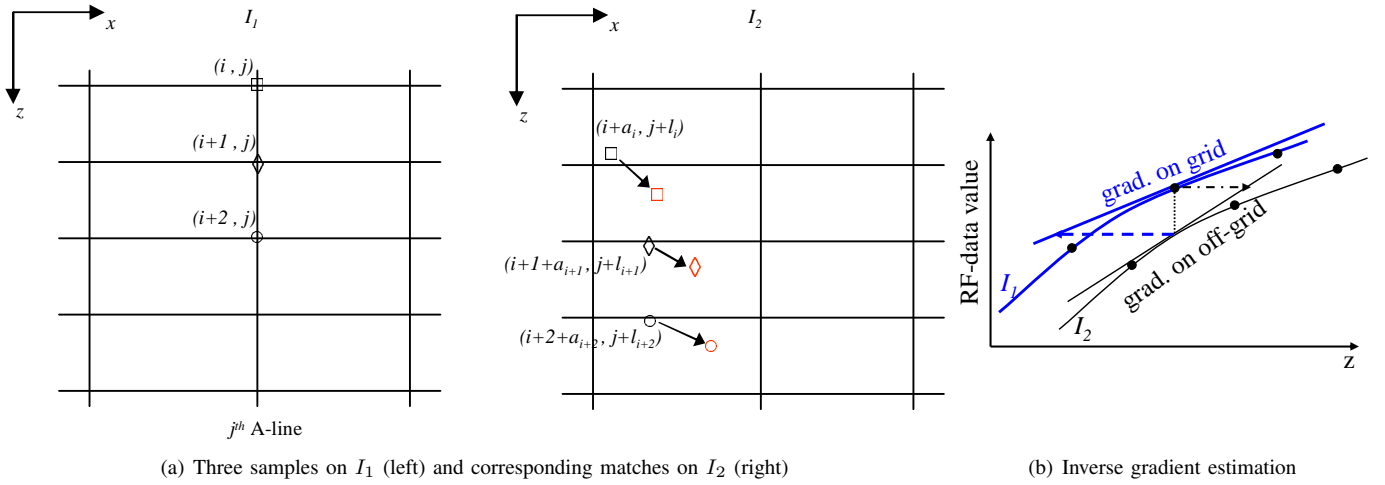


Fig. 2. Schematic plot of subsample tissue motion. (a) In I_2 the initial estimates (in black) are updated by the arrows (three components of $\Delta \mathbf{d}$) to new estimates (in red) after an iteration of 2D AM. To find $\Delta \mathbf{d}$ using Equation 19, it is required to calculate image gradient at the off-grid initial estimate locations (in black) on I_2 . (b) Schematic plot of two RF-data I_1 and I_2 , each sampled at three locations (black dots). The black dashed-dotted arrow shows Δa of the sample on I_1 (ignoring the regularization term) which requires calculating the gradient on I_2 at an off-grid location. The blue dashed arrow shows Δa of an off-grid sample on I_2 (ignoring the regularization term) which requires calculating the gradient on I_1 at an on-grid location. Ignoring second order derivatives, the length of the two arrows is equal.

strain field is discontinuous. We use the prior of piecewise strain continuity via a Kalman filter to improve the quality of strain estimation. Although locations with strain discontinuity are limited, we will develop a technique to take such discontinuities into account.

We first calculate the strain using least squares regression. Each RF-line is first differentiated independently: for each sample i , a line is fitted to the displacement estimates in a window of length $2k + 1$ around i , i.e. to the samples $i - k$ to $i + k$. The slope of the line, $z_{i,j}$, is calculated as the strain measurement at i . The center of the window is then moved to $i + 1$ and the strain value $z_{i+1,j}$ is calculated. We reuse overlapping terms in calculation of $z_{i,j}$ and $z_{i+1,j}$, and therefore the running time is independent of the window length $2k+1$. Having $z_{i,j}$ for $i = 1 \dots m$ and $j = 1 \dots n$, we propose the following algorithm based on Kalman filter to take into account the prior of strain continuity.

$z_{i,j}$ are the noisy measurements of the underlying strain field $\epsilon_{i,j}$. Since the $z_{i,j}$ values are calculated using axial windows, we apply the Kalman filter in the lateral direction. Let r_j be the Gaussian process noise and s_j be the Gaussian measurement noise to be removed. We have [52], [41]

$$\epsilon_{i,j} = \epsilon_{i,j-1} + r_{i,j} \quad (21)$$

$$z_{i,j} = \epsilon_{i,j} + s_{i,j} \quad (22)$$

Let $\hat{\epsilon}_{i,j}^-$ (note the super minus) be our *a priori* strain estimate from the process prior to step j (i.e. from the Equation 21) and $\hat{\epsilon}_{i,j}$ be our *a posteriori* strain estimate at step j given measurement z_j . Let also the variances of $\hat{\epsilon}_{i,j}^-$ and $\hat{\epsilon}_{i,j}$ be respectively p^- and p . The time update (i.e. prior estimation) equations will be [41]

$$\hat{\epsilon}_{i,j}^- = \hat{\epsilon}_{i,j-1} \quad (23)$$

$$p_{i,j}^- = p_{i,j-1} + \sigma_r^2 \quad (24)$$

where σ_r^2 is the variance of the process noise r . $p_{i,j-1}$ is initialized to zero for the first sample $j = 1$. The measurement update equations will be [41]

$$\hat{\epsilon}_{i,j} = \hat{\epsilon}_{i,j}^- + \frac{p_{i,j}^-}{p_{i,j}^- + \sigma_s^2} (z_{i,j} - \hat{\epsilon}_{i,j}^-) \quad (25)$$

$$p_{i,j} = \left(1 - \frac{p_{i,j}^-}{p_{i,j}^- + \sigma_s^2}\right) p_{i,j}^- \quad (26)$$

where σ_s^2 is the variance of the measurement noise s . Note that since both the state $\epsilon_{i,j}$ and measurement $z_{i,j}$ are scalars, all the update equations only require scalar operations. We estimate σ_r^2 and σ_s^2 as following. Let the mean (calculated using a Gaussian kernel of standard deviation of $\sigma_G = 0.6$ sample) of the strain values in 3×3 blocks around samples $(i, j - 1)$ and (i, j) be μ_{j-1} and μ_j respectively. Then σ_r^2 is [52]

$$\sigma_r^2 = (\mu_{j-1} - \mu_j)^2. \quad (27)$$

This is a reasonable estimate of σ_r^2 as it tries to capture the difference between pixel values at adjacent RF-lines. If the difference between the mean strain values is high, less weight is given to the *a priori* estimate. This space-variant estimation of the model noise provides a better match to local variations in the underlying tissue leading to a greater noise reduction. σ_s^2 is the variance of $z_{i,j}$ measurements in the entire image and is constant throughout the image.

The strain estimation algorithm can be summarized as following:

- 1) Perform least squares regression in the *axial* direction for each RF-line. Generate a (noisy) strain image Z whose pixel i, j is $z_{i,j}$. This step ensures continuity in the axial direction.

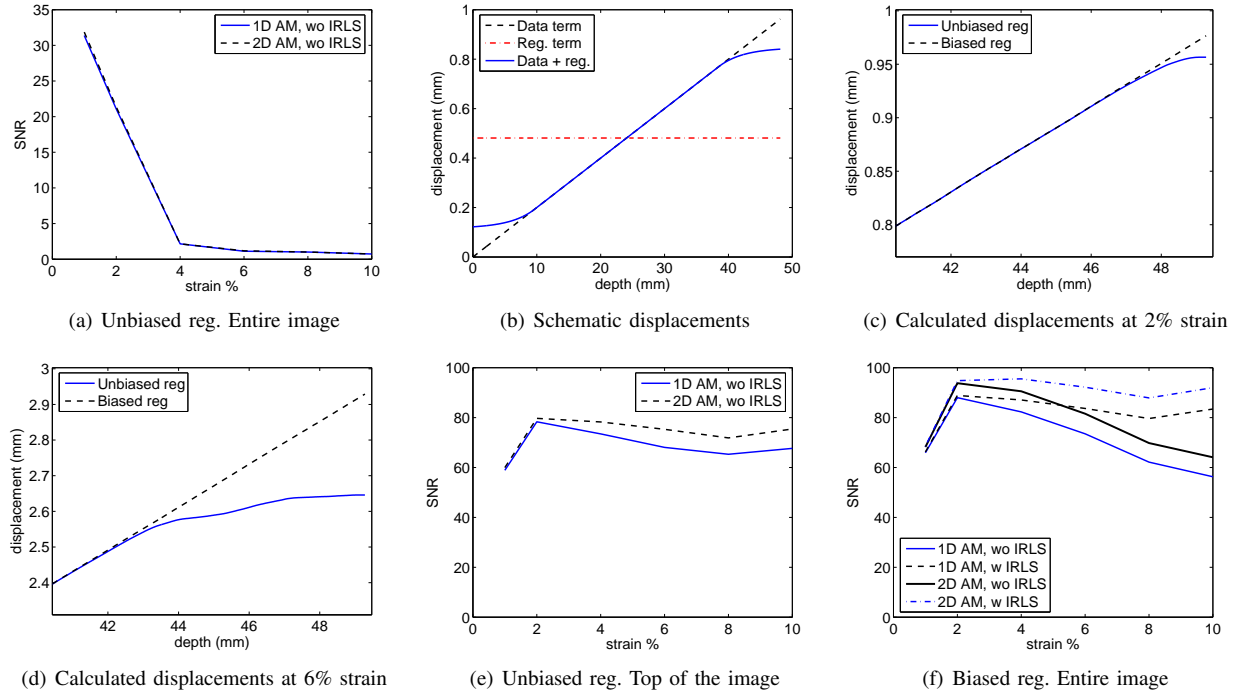


Fig. 3. Axial strain estimation in the first simulated phantom. (a) The SNR values corresponding to the unbiased regularization calculated in the entire image. (b) Schematic plot showing the underestimation of the displacement (Data + reg. curve) with unbiased regularization (refer to the text). (c)-(d) The calculated displacements at the bottom of a RF-line at 2% strain and 6% strain levels respectively with biased and unbiased regularization terms. *The ground truth matches the displacement given by the biased regularization almost perfectly, and therefore is not shown in (c) and (d) not to block the biased regularization results.* The length of the RF-line is 2560 (49.3 mm). (e) The SNR values corresponding to the unbiased regularization calculated by omitting the bottom 300 samples of the image. (f) The SNR values corresponding to the biased regularization calculated in the entire image. Note that the scale of the SNR in graph (a) is much smaller than that of graphs (e) and (f).

- 2) Apply the Kalman filter to the noisy strain image Z in the *lateral* direction. Generate a (denoised) strain image whose pixel i, j is $\hat{\epsilon}_{i,j}$. This step ensures continuity in the lateral direction.

Both steps are applied once and are not iterated. We show in the experimental results how the Kalman filter removes the noise from the strain image with minimal blurring, owing to the model noise update Equation 27.

III. SIMULATION RESULTS

Field II [53] and ABAQUS (Providence, RI) software are used for ultrasound simulation and for finite element simulation. Many scatterers are distributed in a volume and an ultrasound image is created by convolving all scatterers with the point spread function of the ultrasound and adding the results using superposition. The phantom is then meshed and compressed using finite element simulation, giving the 3D displacement of each node of the mesh. The displacement of each scatterer is then calculated by interpolating the displacement of its neighboring nodes. Scatterers are then moved accordingly and the second ultrasound image is generated. The displacement and strain fields are then calculated using the AM methods and are compared with the ground truth. The unitless metric signal to noise ratio (SNR) and contrast to noise ratio (CNR) are also calculated to assess the performance of the

AM method according to

$$\text{CNR} = \frac{C}{N} = \sqrt{\frac{2(\bar{s}_b - \bar{s}_t)^2}{\sigma_b^2 + \sigma_t^2}}, \quad \text{SNR} = \frac{\bar{s}}{\sigma} \quad (28)$$

where \bar{s}_t and \bar{s}_b are the spatial strain average of the target and background, σ_t^2 and σ_b^2 are the spatial strain variance of the target and background, and \bar{s} and σ are the spatial average and variance of a window in the strain image respectively.

The parameters of the ultrasound probe are set to mimic commercial probes. The probe frequency is 7.27 MHz, the sampling rate is 40 MHz and the fractional bandwidth is 60%. A Hanning window is used for apodization, the single transmit focus is at 22.5 mm, equi-distance receive foci are from 5 mm to 45 mm at each 5 mm, the transmit is sequential, and the number of active elements is 64.

Two simulated phantoms are generated. The first phantom is $50 \times 10 \times 55$ mm and the second one is $36 \times 10 \times 25$ mm. Respectively 5×10^5 and 1.4×10^5 scatterers with Gaussian scattering strengths [54] are uniformly distributed in the first and second phantom, ensuring more than 10 scatterers [55] exist in a resolution cell.

The mechanical properties of both phantoms, required for finite element simulation, is assumed to be isotropic and homogeneous. The first phantom is uniform while the second phantom contains a circular hole filled with blood that can move out-of-plane, simulating a blood vessel in tissue (Figure 7 (a)). The scatterers are distributed in the vessel, also with the

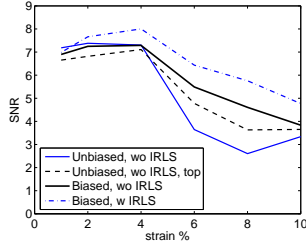


Fig. 4. Lateral strain estimation using the 2D AM method in the first simulated phantom.

same intensity and distribution as the surrounding material. A uniform compression in the z direction is applied and the 3D displacement field of phantoms is calculated using ABAQUS. The Poisson's ratio is set to $\nu = 0.49$ in both phantoms to mimic real tissue [56], [57], which causes the phantoms to deform in x & y directions as a result of the compression in the z direction.

The first phantom undergoes compressions in the z direction to achieve strain levels of 1% to 10%. Figure 3 shows the SNR of the axial strain of the 1D AM and 2D AM methods (the window for SNR calculation covers the entire strain image in (a) & (f)). The sharp drop of the SNR with strain in graph (a) is mainly due to the strain underestimation in the bottom part of the image. It can be explained as following. The unbiased regularization term tries to force constant displacement (dashed-dotted red line in (b)). Assuming an ideal noiseless case where the data term gives a smooth ramp displacement (dashed black line in (b)), minimizing the cost function (which is the summation of the data and the regularization terms) will underestimate the displacement at the two ends (solid blue line in (b)). This underestimation decays exponentially moving towards the center of the image. This artifact is shown in the simulation experiment at 2% and 6% strain levels in (c) and (d). Since we exploit the fact that the axial displacement of the first sample is zero (Section II-C), the underestimation does not happen in the top of the image. Biasing the regularization prevents this artifact, as is shown in (c) and (d). The AM method with or without the bias term gives the same result away from the bottom of the image: part (e) shows that if we ignore 300 (5.8 mm) samples at the bottom of the image, the SNR will not drop sharply unlike in part (a). Part (f) shows the SNR of the AM methods with biased regularization calculated in the entire image. The SNR at 1% strain in parts (e) and (f) is the same. At higher strain levels, the strain underestimation propagates more into the middle of the image, and therefore the SNR decreases at higher strain levels in graph (e). Part (e) shows 2D AM gives slightly better axial strain compared to 1D AM. IRLS slightly increases the SNR. However, we will see in the simulation results of the second phantom that in the presence of outliers significant improvement in SNR and CNR is achieved using IRLS.

The SNR of the lateral strain field is much lower than that of the axial strain field (Figure 4). Unbiased regularization gives the lowest SNR, mainly due to artifacts in the bottom of the image. Similar to the axial strain, the SNR improves as 300

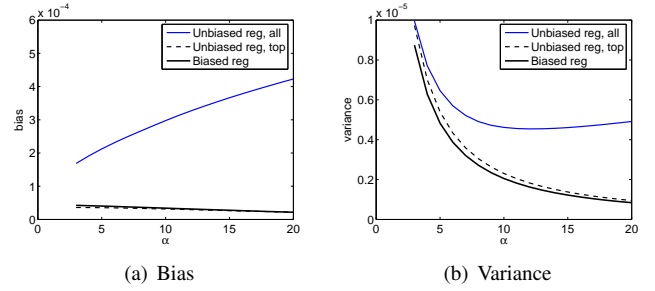


Fig. 5. Bias and Variance of the axial strain as a function of the axial regularization weight α . The ground truth axial and lateral strain fields are respectively uniform 2% and $2\nu\%$ fields ($\nu = 0.49$ is the Poisson's ratio). The solid blue and dashed black curves both correspond to unbiased regularization and the solid black curve corresponds to the biased regularization. In the solid blue and solid black curves, the entire image is included in the calculation of the bias and noise. In the dashed black curve the bottom part of the strain field which suffers from high bias (Figure 3 (b)) is excluded from the calculation of the bias and noise. 1D AM and 2D AM have very similar bias and variance. The curves with and without IRLS are also very close. Therefore each curve corresponds to 1D AM or 2D AM with or without IRLS.

samples from the bottom of image are omitted from the SNR calculation (results not shown).

The effect of the regularization weights on bias and variance of the axial strain image at 2% ground truth axial strain is shown in Figure 5. The blue curves show the bias and variance of the entire strain image obtained with unbiased regularization. It shows the tradeoff between the bias and variance: increasing the regularization weight increases the bias and decreases the variance. The variance starts to increase at $\alpha \approx 12$ which is caused by the underestimation of the strain at the bottom of the image (the artifact in Figure 3 (c)). If we exclude the bottom 300 samples of the strain image from the bias and variance calculation (the black dashed curve), we see a consistent drop of variance as α is increased. The black curves show the bias and variance of the entire strain image obtained with biased regularization. Biasing the regularization causes the bias to decrease as the regularization weight α is increased which is a nonstandard behavior. It can be explained by the simple ground truth strain field which is uniform, exactly what the regularization term is trying to achieve. Even in the unbiased case, only the bias of the bottom part of the strain field increases as α is increased (i.e. in the bias plot, the blue curve increases while the black dashed curve decreases). Therefore, one cannot conclude from this experiment that higher α is beneficial to both bias and variance. To prove this, we designed a simulation study where the underlying axial strain field continuously varied with depth and the lateral and elevational strains were zero (such strain field is not physically realizable). We observed that the absolute value of the bias monotonically increases with α with both unbiased and biased regularizations. To save space, we do not present the full results here. Similar curves for the lateral strain field is shown in Figure 6.

The second simulation experiment is designed to show the effect of smoothness weight and IRLS threshold CNR when the correlation is lower in parts of the image due to fluid motion. The phantom contains a vein oriented perpendicular to the image plane (Figure 7). The background window for

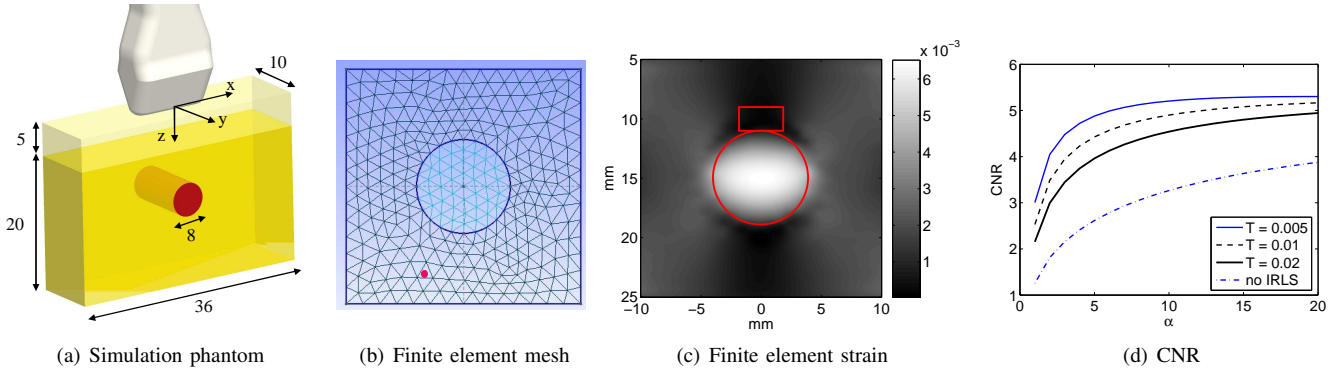


Fig. 7. Second simulation experiment. Measurements in (a) are in mm. In (b), a scatterer is shown in the bottom left part as a red dot. Its displacement is calculated by interpolating the displacements of its 3 neighboring nodes on the mesh. The target (circular) and background (rectangular) windows for CNR calculation of (d) are shown in (c).

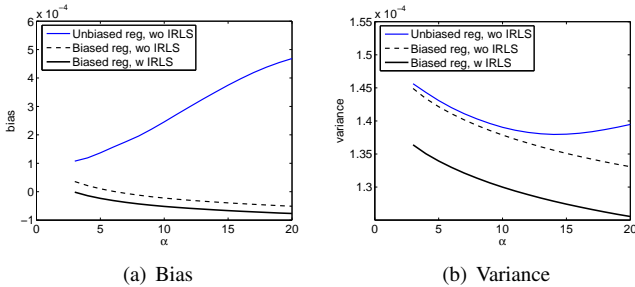


Fig. 6. Bias and Variance of the lateral strain as a function of the axial regularization weight α . The ground truth axial and lateral strain fields are respectively uniform 2% and $2\nu\%$ fields ($\nu = 0.49$ is the Poisson's ratio). The solid blue curve corresponds to unbiased regularization and the dashed and solid black curves correspond to the biased regularization. IRLS is not used in the solid blue and dashed black curves.

CNR calculation is located close to the target window to show how fast the strain is allowed to vary, a property related to the spatial resolution. The maximum CNR with IRLS is 5.3 generated at $T = 0.005$ and $\alpha_a = 38$, and without IRLS is 4.8 at $\alpha_a = 338$. Such high α_a value makes the share of the data term in the cost function very small and causes over-smoothing.

A. Displacement Simulation

To study the performance of the Kalman filter, we simulate a displacement field of size 100×100 samples whose strain image (calculated using least squares regression) is as shown in Figure 8 (a). 100 samples in the axial direction corresponds to approximately 1.9 mm (assuming 40 MHz sampling rate), and 100 samples in the lateral direction corresponds to 10 mm to 25 mm depending on the probe. To be consistent with the notations of Section II-D, let $\epsilon_{i,j}$ denote the strain values of the uncontaminated image in (a). We then contaminate the displacement field with a Gaussian noise with standard deviation of 1.5 samples, and perform least squares regression to calculate the noisy estimates $z_{i,j}$ (Figure 8 (b)). We then apply the Kalman filter as described in Section II-D to the

noisy estimates $z_{i,j}$ in the lateral direction (i.e. row-by-row). The posterior estimates of the strain values, $\hat{\epsilon}_{i,j}$ are shown in (c). The strain values of the shown line in (a) - (c) (at $i = 50$ samples) is shown in (d) and (e) (The plot in (d) around the step in magnified in (e)). The Kalman filter formulation is eliminating the noise without over-smoothing the strain image. This is due to the model variance update Equation 27. We note that although displacement is generally continuous in tissue, its spatial derivation (strain) is not: at the boundary of two tissues with different elasticity moduli, strain field is discontinuous.

IV. EXPERIMENTAL RESULTS

For experimental evaluation, RF data is acquired from an Antares Siemens system (Issaquah, WA) at the center frequency of 6.67 MHz with a VF10-5 linear array at a sampling rate of 40 MHz. Only the 2D AM method is used in the experimental results. Phantom results and patient trials are presented in this section. The tunable parameters of the 2D AM algorithm are set to $\alpha = 5$, $\beta_a = 10$, $\beta_l = 0.005$ and $T = 0.2$ (Equations 12 & 20), and the tunable parameters of the DP (run for the seed RF-line in the 2D AM algorithm) are $\alpha_a = \alpha_l = 0.15$ (Equation 1) in all the phantom results (except if specified otherwise). In the patient results, all the parameters are the same except for β_a which is increased to $\beta_a = 20$ because the data is noisier. The strain images in all the patient trials are obtained using the least squares regression and Kalman filtering as described in Section II-D.

A. Phantom Results

1) *Effect of Regularization on Residuals:* The cost function of the AM method (Equation 7) is composed of residuals (i.e. the data term) and the regularization terms. The AM method minimizes this summation. Therefore the AM method will not necessarily minimize the residuals. We now show that the data term alone is non-convex and has many local minima. Adding the regularization term will eliminate many of the local minima and makes optimization of the data term easier. This

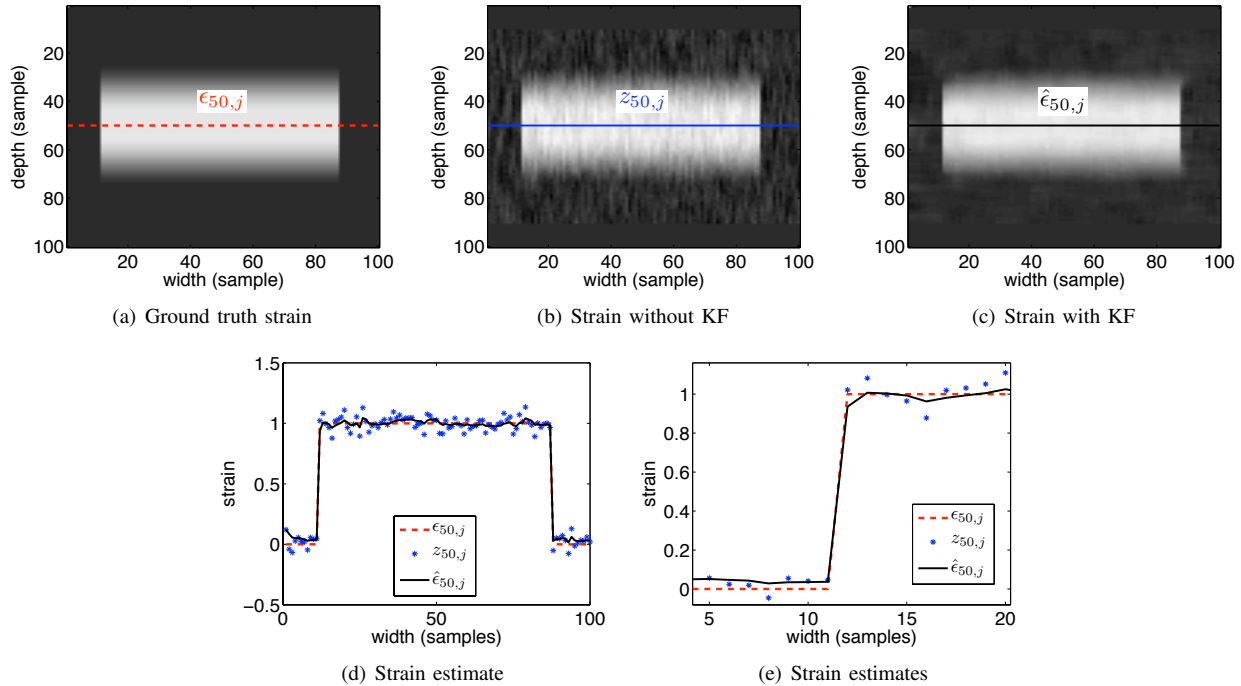


Fig. 8. Performance of the least squares regression and the Kalman filter on simulated motion data. (a) shows the strain field calculated using least squares regression of the uncontaminated displacement field. (b) depicts the strain field calculated using least squares regression of the contaminated displacement field. (c) shows the strain field calculated from the noisy measurements of (b) using the proposed Kalman filter (KF in (b) and (c) refers to Kalman filter). The pixels of images in (a) to (c) are respectively the ground truth (unavailable) strain values $\epsilon_{i,j}$, the noisy measurements $z_{i,j}$, and posterior strain values $\hat{\epsilon}_{i,j}$. The brightness scale in (a) to (c) is the same. (d)-(e) are the strain estimation at the horizontal line shown in (a) to (c). (d) is magnified in (e) around the step. The Kalman filter removes the noise while keeping the image sharp, due to the variable model noise of Equation 27.

is in addition to the effect of regularization that makes the displacement field smooth, a generally desired attribute.

The effect of regularization on the residuals is studied using experimental data. An elastography phantom (CIRS elastography phantom, Norfolk, VA) is compressed 0.2 in axially using a linear stage, resulting in an average strain of 6%. Two RF frames are acquired corresponding to before and after the compression. The Young's elasticity modulus of the background and the lesion under compression are respectively 33 kPa and 56 kPa. The displacement map is calculated using the 2D AM method and the residuals corresponding to the displacement map are obtained. Figure 9 (a)-(c) shows the axial and lateral strains at such a high strain rate (minimum of 2% and maximum of 11%). The mean and median of the residuals $\rho(r_i)$ in the entire image is shown in (d). One could expect the graph to monotonically increase as the regularization weight α increases, since the difference between the objective function C and the residuals $\sum_{i=1}^m \rho(r_i)$ is increased as α is increased. However, the residual values are very high at very low α . Therefore, numerical minimization of $\sum_{i=1}^m \rho(r_i) + R(\Delta \mathbf{d})$ gives a smaller value for $\sum_{i=1}^m \rho(r_i)$ compared to trying to directly minimize $\sum_{i=1}^m \rho(r_i)$. This indicates that the nonregularized cost function is not quasi-convex and is very hard to minimize.

2) *Resolution of the Strain Images Generated with AM:* The effect of the regularization on spatial resolution is evaluated experimentally using the experimental setup of the previous experiment. The compression is set to 0.1 in in this experiment.

Figure 10 (a) shows the strain image obtained by compression the lesion with the Young's modulus of 56 kPa. Spatial resolution is evaluated using modulation transfer function (MTF), an established method for estimating the spatial resolution of medical imaging systems that was relatively recently extended to elastography [58]. The spatial resolution of the reconstructed images is determined with a three-step approach [59], [60]; first, the edge spread function is computed by averaging the pixel values across the background-inclusion interface (the line in Figure 10 (a)); second, the line spread function (LSF) is computed by differentiating the edge spread function; third, the MTF is determined by computing the Fourier transform of the LSF and normalizing the resulting function to zero spatial frequency:

$$\text{MTF}(k) = \frac{\Xi(k)}{\Xi(0)} \quad (29)$$

Figure 10 (c) shows the MTF for five different normalization coefficients respectively. Strain results are obtained with a regression window of length $2k + 1 = 65$ (Section II-D). Increasing the regularization weight is adversely affecting spatial resolution. Spatial resolution is defined as the spatial frequency when the value of MTF is 0.1. At $\alpha = 1$, $\alpha = 2$ and $\alpha = 4$ this value is respectively 2 cycles/mm, 1 cycles/mm and 0.5 cycles/mm. In addition to α , this value also depends on the length of the regression window $2k + 1$.

3) *Image Quality Versus Axial and Lateral Sampling Rates of the RF-Data:* Sampling rate of the RF-data usually ranges from 20 MHz to 50 MHz depending on the hardware of the

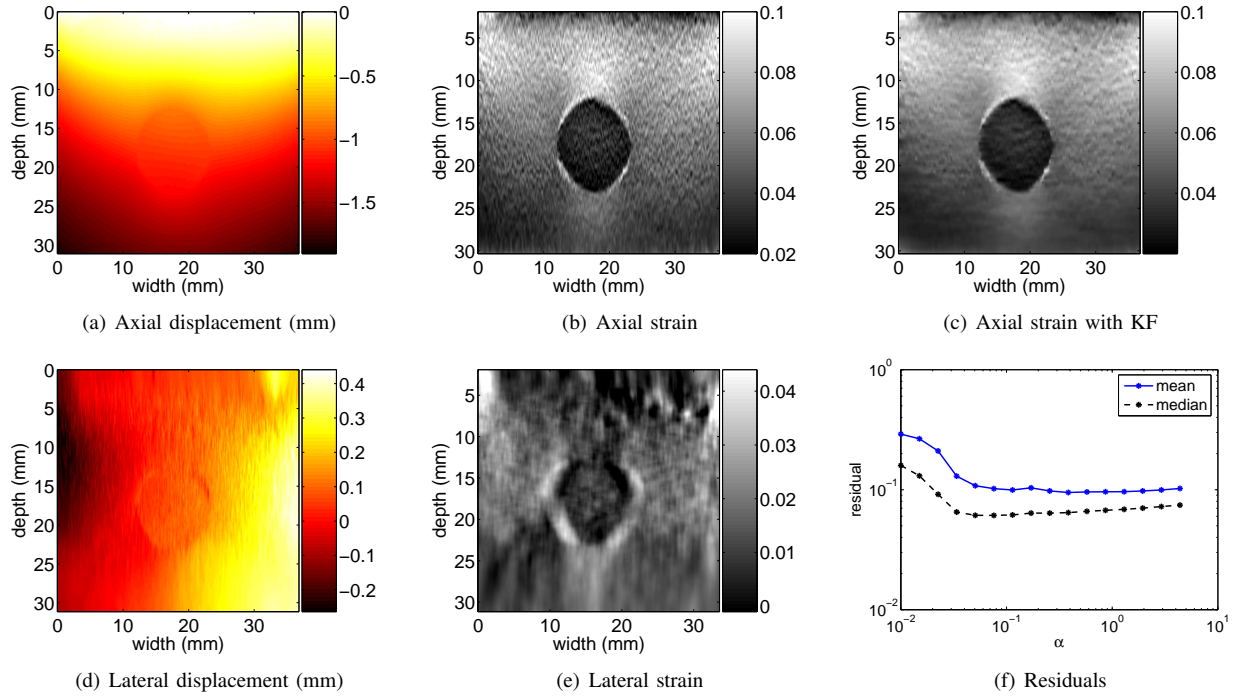


Fig. 9. Phantom experimental results. The top row shows axial displacement and axial strains as labeled (KF in (c) refers to Kalman filter). Average axial strain and maximum strain are approximately 6.6% and 11%. (d) and (e) show lateral displacement and lateral strain respectively. (f) shows residuals as the regularization weight varies.

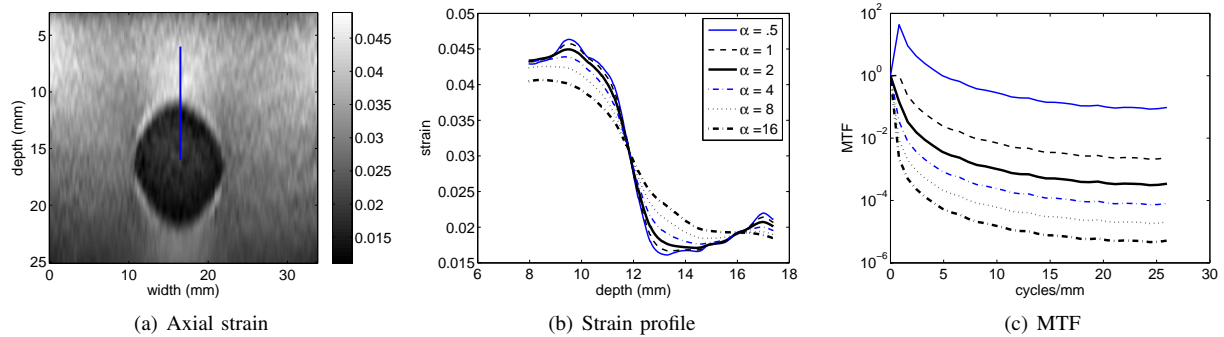


Fig. 10. Phantom experimental results showing the resolution of the 2D AM. (a) Strain image. The edge spread function is evaluated along the vertical line. (b) The strain across the edge (vertical line in (a)) for the five shown regularization values. (c) The MTF calculated across the vertical line in (a). Spatial resolution is defined as the spatial frequency when the value of MTF is 0.1.

device. The number of the A-lines provided in an image also varies significantly. In addition, bandwidth limitations of the data transfer can impose limits on the size of the image for real-time operations. In this study, we downsample the RF-data by a factor of 2 to 4 in the axial direction and by a factor of 2 to 8 in the lateral direction. Figure 11 (a)-(g) shows axial and lateral displacement and strain images of the CIRS elastography phantom undergoing maximum axial strain of 5%. Axial sampling rate can be reduced by a factor of 2 without significant impact on the strain image quality (part (h)). Downsampling the images in the lateral direction by a factor of 4 results the CNR of the axial and lateral strain images to drop respectively 12% (from 16.3 to 14.3) and 56% (from 2.55 to 1.13) as shown in (i). While the axial strain is robust to the number of A-line in the image even at a high

strain level of 5%, the lateral strain is sensitive to it (i). Similar study with lower axial strain levels shows that as the axial strain decreases, higher downsampling rates in both axial and lateral directions are possible without a large impact on the results.

4) *Kalman Filter*: The performance of the Kalman filter is studied using the RF-data used in Figure 9. The linear least squares differentiation technique is applied to the axial displacement field calculated with 2D AM, resulting in $z_{i,j}$ (Figure 12 (a)). The Kalman filter is then applied to $z_{i,j}$ measurements of (a), giving the posterior $\hat{e}_{i,j}$ measurements of (b). Comparing the strain values at a horizontal line of (a) and (b), the noisy $z_{i,j}$ measurements are smoothed in the lateral direction using the proposed Kalman filter, with minimal blurring of the edge.

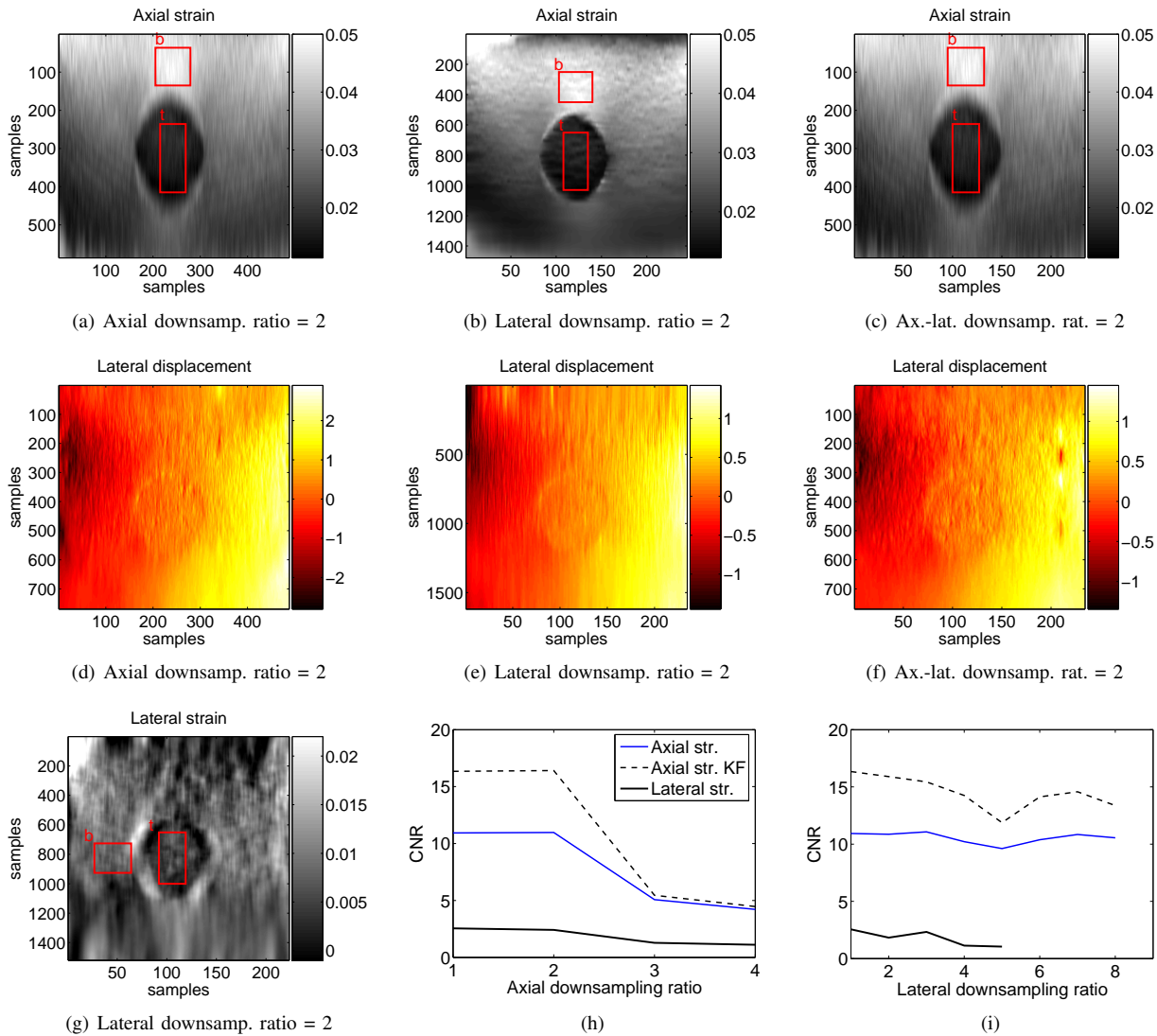


Fig. 11. Results of the CIRS elastography phantom at 5% maximum strain at different axial and lateral sampling rates. The hard lesion is spherical and has a diameter of 1 cm. Downsampling is performed by simply skipping samples in the axial or (and) lateral directions. In (c) & (f), a downsampling ratio of 2 is applied in both axial and lateral directions. The lateral displacement is shown in number of samples in (d) to (f). (h) and (i) show the CNR between the target and background windows in the strain images as the axial or lateral downsampling rates change. The target and background windows are shown in the axial strain images (a) to (c) and the lateral strain image (g). In (i), the lateral strain curve is not calculated for downsampling ratios of 6 and higher because the background window moves out of the image. The black dashed curve with the highest CNR is the strain obtained with the Kalman filter (KF).

B. Clinical Study

Seven patients undergoing open surgical radiofrequency (RF) thermal ablation for primary or secondary liver cancer were enrolled between February 06, 2008 and July 28, 2009. All patients enrolled in the study had unresectable disease and were candidates for RF ablation following review at our institutional multidisciplinary conference. Patients with cirrhosis or suboptimal tumor location were excluded from the study. All patients provided informed consent as part of the protocol, which was approved by the institutional review board. RF ablation was administered using the RITA Model 1500 XRF generator (Rita Medical Systems, Fremont, CA). Strain images are generated offline. Some preliminary results are published in [15].

We show the results from only 4 patients due to space limitations. Figure 13 shows the B-mode scan, the strain

images and CT scans performed after RF ablation. Tissue is simply compressed freehand at a frequency of approximately 1 compression per 2 sec with the ultrasound probe without any attachment. The shadow in Figure 13 (a) at 20 mm depth is produced by the thermal lesion. Note that it is not possible to ascertain the size and position of the thermal lesions from B-mode images. In addition, the thermal lesion has different appearances in the three B-scans. However, the thermal lesions show very well as hard lesions in the strain images. After gross correlation of the post ablation CT scan and the thermal lesion in the strain images, the size of the lesion seems to correspond well. However, a more rigorous validation of the size and shape of the ablated lesion in the elastography image is underway using nonrigid registration of CT and ultrasound images. To the best of our knowledge, this is also the first demonstration of the success of elastography in imaging the

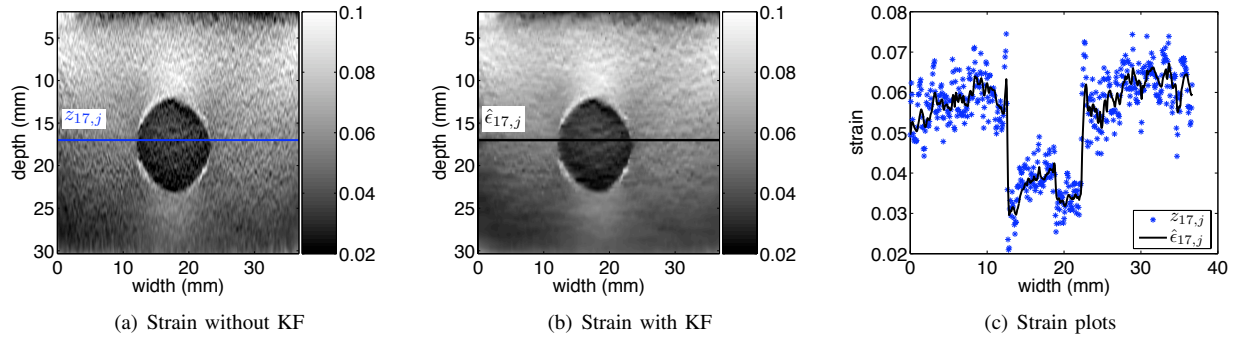


Fig. 12. Performance of the least squares regression and the Kalman filter in experimental data. (a) shows the axial strain field calculated by least squares regression of the noisy displacement field. (b) depicts the strain field calculated from the noisy measurements of (a) using the proposed Kalman filter (KF in (a) and (b) refers to Kalman filter). The pixels of images in (a) and (b) are respectively the least squares measurements $z_{i,j}$, and posterior strain values $\hat{e}_{i,j}$. (c) shows the strain estimation at the 17 mm deep horizontal line shown in (a) to (b). The Kalman filter removes the noise while keeping the image sharp, due to the variable model noise of Equation 27.

thermal lesion in an *in-vivo* human experiment.

We have also acquired patient RF data of liver ablation prior and after ablation in one of the patient trials. Figure 14 shows the B-mode, strain and venous and arterial phase ² CT images obtained before ablation, and Figure 15 shows the B-mode, strain and lateral displacement images after ablation. In Figure 14, the tumor (marked in the CT images (f) and (g)) is not visible in the B-mode image (a), but is clearly visible in the strain images (b) and (c). While the tissue is getting compressed with the ultrasound probe, the middle hepatic vein (marked as 5) which is only 4-8 cm from vena cava inferior pulsates at high amplitude. The graph in (e) schematically shows the probe motion and variations in the diameter of the vein. Therefore, the vein can look soft as in (c) or hard as in (b) depending on whether its diameter variation is in the same (marked by ellipse 1 in (e)) or opposite (marked by ellipse 2 in (e)) direction as the probe motion. The effect of pulsation of vessels, a well-known cause of signal decorrelation, is minimized via IRLS resulting in a low noise strain image. In addition, since the 2D AM method gives a dense motion field (same size as RF data), the small artery at the diameter of less than 2 mm (marked as 4 in (a)) is discernible in (b) from the low pressure portal vein. The ablated lesion is also discernible in the strain images of Figure 15 (b) and (c). We believe the soft region in the middle of the two hard ablation lesions in (b) and (c) (at the depth of 25-30 mm and width of 10-25mm) is not close to any of the 10 times of the ablation probe. Therefore because of its proximity to veins and vessels its temperature has remained low.

V. DISCUSSION

The resolution of the method is formally studied in Section IV-A using the phantom experiment. Future work will include more intuitive measures for resolution in terms of the smallest detectable target as a function of its elasticity difference with the background.

²CT scans are performed at different phases after intravenous injection of a contrast agent. In the arterial phase (directly after injection of a contrast agent) arteries will enhance, whereas in the venous phase (30-60 sec after injection) the hepatic parenchyma and veins will enhance.

The cost function is a regularized function of all displacements on an A-line. This makes the methods robust to noise which exist throughout the image. Besides, the AM methods are not window-based and therefore they don't suffer from decorrelation within the window. As a result, both AM methods work for strains as high as 10%. In addition, the IRLS outlier rejection technique makes the AM methods robust to local sources of decorrelation such as out-of-plane motion of movable structures or blood flow.

Global stretching assumes a constant strain across the depth and stretches one of the RF-lines accordingly. It is shown that it enhances the quality of correlation based elastography methods. The reason is that the strain of each point can be assumed to be the global strain (fixed for each RF-line) plus some perturbation, i.e. constant strain is a better approximation than zero strain. Biasing the regularization is motivated by the same reason and involves almost no additional computational cost.

Improvement in the SNR and CNR achieved with Kalman filtering differentiation is due to utilizing the (piecewise) continuity of the strain field. One could think of a unified framework which includes both the 2D AM and the Kalman filtering and directly calculates the strain field. We made an effort to formulate Equation 15 in terms of strain values. Unfortunately, the coefficient matrix in the L.H.S. became a full matrix for our desired regularization. Such large full system cannot be solved in real-time.

The least squares differentiation of Section II-D can be incorporated in the Kalman filter. This can be simply done by defining the state at each point to be the displacement and the strain of that point. The observed variables are the noisy displacement measurements from 2D AM. Solving for the state gives a strain estimate at each point. However, we preferred to follow the common approach of first finding the strain by solving least squares. In addition, the axial and lateral displacements can be considered as two channels of a measurement and a Kalman filter that takes into account both intra-channel (spatial) and inter-channel variations can be developed. This is a subject of future work.

Lateral displacement estimation with 2D AM is of order of

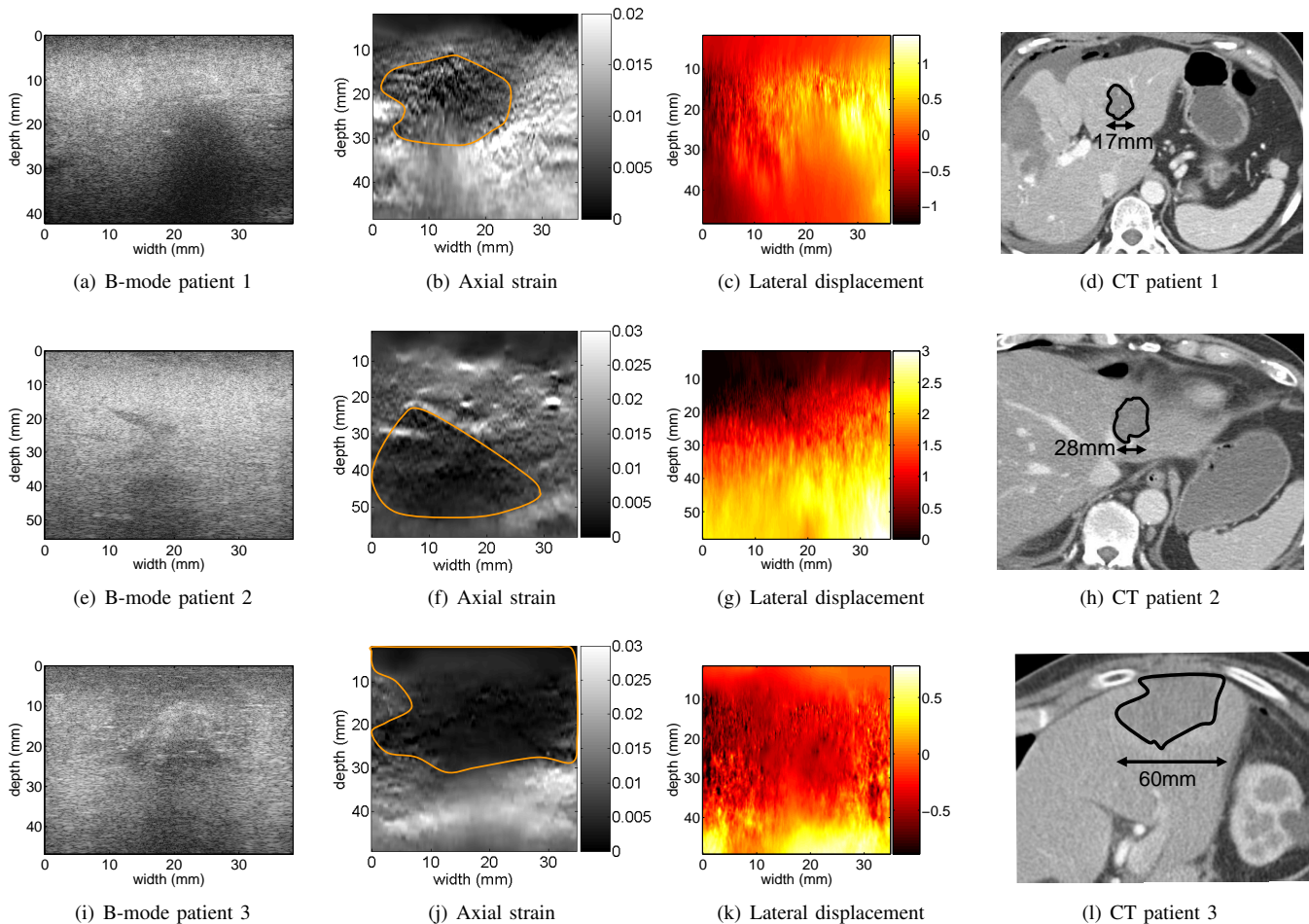


Fig. 13. *In-vivo* images of the thermal lesion produced by RF ablation therapy of liver cancer. All images acquired after ablation. 1st, 2nd and 3rd rows correspond to the 1st, 2nd and 3rd patients respectively. The thermal lesion shows in (b), (f) & (j) as dark, surrounded by normal tissue in white. The lateral displacement images are shown in number of samples (they do not immediately carry anatomical information). In (b), (d), (f), (h), (j) & (l) the delineated thermal lesions is shown. The non-unity aspect ratio in the axes of the B-mode and strain images should be considered when comparing them to the CT scans.

magnitude less accurate than the axial displacement estimates. We tested the following algorithm for calculating the lateral displacement field based on 1D AM: run 1D AM to find the axial displacement field A , then transpose both ultrasound images I_1 and I_2 and run 1D AM again using A calculated in the previous step. The axial displacement field calculated for the transposed images is in fact the lateral displacement of the original images. Although considerably more computationally expensive than 2D AM, this algorithm did not improve the lateral displacement estimation. Therefore only images of lateral displacement are provided for the patient trials because the lateral strain did not show the ablation lesion. This is in accordance with recent work [36] which only shows the lateral displacement. A 2D displacement field can be utilized to calculate the thermal expansion and to reconstruct the strain tensor. Incorporation of the synthetic lateral phase [61], [62], [63] into 2D AM to further improve the accuracy of the lateral displacement measurement is also a subject of future work.

In cases where the two ultrasound frames correlate very poorly throughout the image, 1D AM outperforms 2D AM because DP is run for the entire image in 1D AM. However,

in those cases the strain images are of very low quality even with 1D AM. In cases where the images correlate reasonably, the 2D AM algorithm slightly outperforms 1D AM in terms of the SNR of the axial strain as shown in Figure 3 (e) and (f). Also, 1D AM and 2D AM are very similar in terms of bias and variance as mentioned in the caption of the Figure 5. And finally, 2D AM is more than 10 times faster than 1D AM because it eliminates the redundant calculations in the DP step of 1D AM. This is important considering that there are combinatorial many ways of choosing two frames for elastography from a sequence of images. Having a fast algorithm, like 2D AM, makes it plausible to invest time to perform real-time frame selection, an area that we are currently working on [16], [64].

Recent work [65] has attempted to reconstruct elasticity from the displacement field for monitoring thermal ablation. It has also shown that [66] compared to strain images, elasticity images have both higher correlation with the ablation zone and give higher CNR. Another work [67] has utilized the solution of the elasticity reconstruction to improve motion estimation in an iterative framework. Calculation of the elasticity modulus

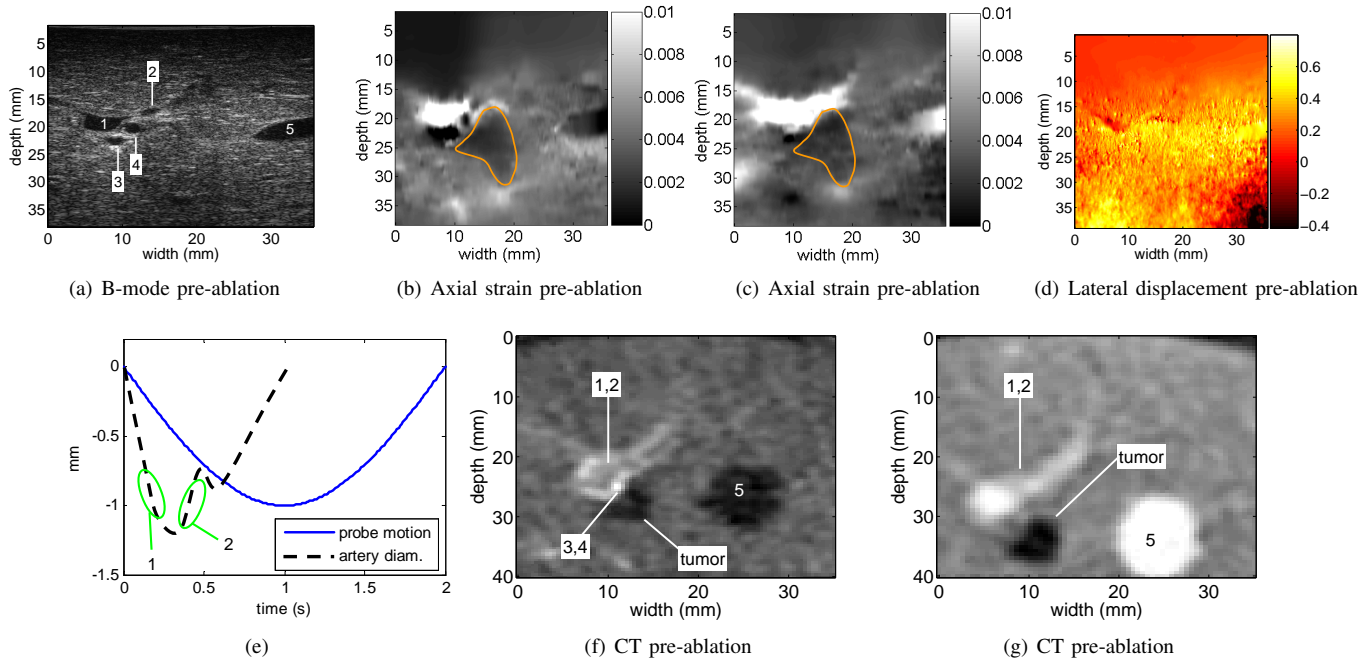


Fig. 14. *In-vivo* images of the fourth patient before RF ablation. In (a), the left anterior branch of portal vein is marked as 1 and 2 and has low pressure and therefore compresses easily. Arteries (marked as 3 and 4) and the middle hepatic vein (marked as 5) however pulsate with the heart beat and may have low or high pressure. (b) and (c) both show the axial strain from the same location before ablation. They are calculated at two different phases of the heart beat. The cancer tumor is discernible in (b) and (c) (regardless of the systolic or diastolic blood pressure), and its boundary is shown. 1 and 2 (as marked in (a)) correspond to the high strain area in both (b) and (c). Since 3, 4 and 5 (as marked in (a)) pulsate, they may look hard (as in (b)) or soft (as in (c)). (d) shows the lateral displacement. The tumors is not visible in this image. (e) shows the motion of the probe and the variation in the diameter of the arteries due to the heart beat (refer to the text). (f) is the arterial phase and (g) is the venous phase contrast CT images. The numbers 1-5 mark the same anatomy as (a).

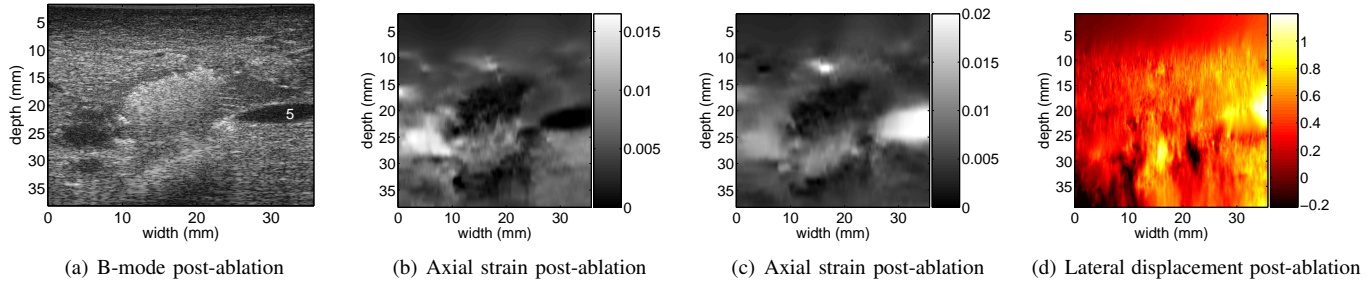


Fig. 15. *In-vivo* images of the fourth patient after RF ablation. Similar to Figure 14, the hepatic vein (marked as 5) can have low strain (as in (b)) or high strain (as in (c)) values.

in our ablation monitoring trials is an area of future work.

Statistical analysis of the residuals is a subject of future work. The sum of squared differences used as the similarity metric in our cost function is suitable if ultrasound noise can be modeled as additive Gaussian noise. However, ultrasound noise is not simply additive Gaussian and it has been shown that similarity metrics that model the noise process considering physics of ultrasound give more accurate results [68]. Performance of the 2D AM method for images that are not fully developed speckles (i.e have few scatterers per resolution cell) is also a subject of future work.

Current implementations of the 1D AM and 2D AM take respectively 0.4 sec and 0.04 sec to generate strain images (axial for 1D AM and axial and lateral for 2D AM) of size 1000×100 on a 3.8 GHz P4 CPU. DP contributes to more than 90% of the running time of the 1D AM, and that's why

it is slower than 2D AM where DP is only run for a single A-line. The running time of both methods changes linearly with the size of the image.

VI. CONCLUSION

Two regularized elastography methods, 1D AM and 2D AM, are introduced for calculating the motion field between two ultrasound images. They both give dense subsample motion fields (1D AM gives subsample axial and integer sample lateral and 2D AM gives subsample axial and lateral) in real-time. The size of the motion fields is the same as the size of the RF-data (except for few samples from the boundary whose displacements are not calculated). Such dense motion fields lead to dense strain fields which are critical in detecting small lesions. The prior of tissue motion continuity is exploited in the AM methods to minimize the effect of signal decorrelation.

The regularization term is biased with the average strain in the image to minimize underestimation of the strain values. Parts of the image that have very low correlation are treated as outliers and their effect is minimized via IRLS. The strain image is calculated by differentiating the motion fields using least squares regression and Kalman filtering. The performance of the proposed elastography algorithms is analyzed using Field II and finite element simulations, and phantom experiments. Clinical trials of monitoring RF ablation therapy for liver cancer in four patients are also presented. An implementation of the 2D AM method, the least squares regression and the Kalman filter in MATLAB mex functions, as well as some of the phantom and patient RF data used in this work are available for academic research and can be downloaded from http://www.cs.jhu.edu/~rivaz/Ultrasound_Elastography/.

ACKNOWLEDGMENT

The authors would like to thank Pezhman Foroughi, Ioana Fleming and Mark van Vledder for valuable discussions, and anonymous reviewers for their constructive feedback. We also acknowledge Johns Hopkins Radiology Department for intramural fundings.

REFERENCES

- [1] K. Parker, L. Taylor, S. Gracewski, and D. Rubens, "A unified view of imaging the elastic properties of tissue," *J. Acoust. Soc. Amer.*, vol. 117, pp. 2705–2712, May 2005.
- [2] J. Greenleaf, M. Fatemi, and M. Insana, "Selected methods for imaging elastic properties of biological tissues," *Annu. Rev. Biomed. Eng.*, vol. 5, pp. 57–78, Apr. 2003.
- [3] J. Ophir, S. Alam, B. Garra, F. Kallel, E. Konofagou, T. Krouskop, and T. Varghese, "Elastography," *Annu. Rev. Biomed. Eng.*, vol. 213, pp. 203–233, Nov. 1999.
- [4] L. Gao, K. Parker, R. Lerner, and S. Levinson, "Imaging of the elastic properties of tissue - a review," *Ultrasound Med. Biol.*, vol. 22, no. 8, pp. 959–977, Aug. 1996.
- [5] K. Hiltawsky, M. Kruger, C. Starke, L. Heuser, H. Ermert, and A. Jensen, "Freehand ultrasound elastography of breast lesions: Clinical results," *Ultrasound Med. Biol.*, vol. 27, pp. 1461–1469, Nov. 2001.
- [6] M. Doyley, J. Bamber, F. Fuechsel, and N. Bush, "A freehand elastographic imaging approach for clinical breast imaging: System development and performance evaluation," *Ultrasound Med. Biol.*, vol. 27, pp. 1347–1357, 2001.
- [7] M. Yamakawa, N. Nitta, T. Shiina, T. Matsumura, S. Tamano, T. Mitake, and E. Ueno, "High-speed freehand tissue elasticity imaging for breast diagnosis," *Jpn. J. Appl. Phys.*, vol. 42, no. 5B, pp. 3265–3270, May 2003.
- [8] T. Hall, Y. Zhu, and C. Spalding, "In vivo real-time freehand palpation imaging," *Ultrasound Med. Biol.*, vol. 29, pp. 427–435, Mar 2003.
- [9] J. Lindop, G. Treece, A. Gee, and R. Prager, "3D elastography using freehand ultrasound," *Ultrasound Med. Biol.*, vol. 32, pp. 529–545, Apr. 2006.
- [10] E. Turgay, S. Salcudean, and R. Rohling, "Identifying the mechanical properties of tissue by ultrasound strain imaging," *Ultrasound Med. Biol.*, vol. 32, no. 2, pp. 221–235, Feb. 2006.
- [11] A. Lorenz, H. Sommerfeld, M. Garcia-Schurmann, S. Philippou, T. Senge, and H. Ermert, "A new system for the acquisition of ultrasonic multicompression strain images of the human prostate in vivo," *IEEE Trans. Ultrason. Ferroelectr. Freq. Control*, vol. 46, pp. 1147–1154, Sept. 1999.
- [12] E. Konofagou, J. D'hooge, and J. Ophir, "Myocardial elastography-a feasibility study in vivo," *Ultrasound Med. and Biol.*, vol. 28, no. 4, pp. 475–482, Apr. 2002.
- [13] J. Rubin, S. Aglyamov, T. Wakefield, M. O'Donnell, and S. Emelianov, "Internal displacement and strain imaging using ultrasound speckle tracking," *IEEE Trans. Ultrason. Ferroelectr. Freq. Control*, vol. 22, pp. 443–448, 2003.
- [14] T. Varghese, J. Zagzebski, and F. Lee, "Elastography imaging of thermal lesion in the liver following radio frequency ablation: Preliminary results," *Ultrasound Med. Biol.*, vol. 28, no. 11, pp. 1467–1473, 2002.
- [15] H. Rivaz, I. Fleming, L. Assumpcao, G. Fichtinger, U. Hamper, M. Choti, G. Hager, and E. Boctor, "Ablation monitoring with elastography: 2d in-vivo and 3d ex-vivo studies," *Medical Image Computing & Computer Assisted Interventions, MICCAI, New York, NY*, pp. 458–466, Sept. 2008.
- [16] H. Rivaz, P. Foroughi, I. Fleming, R. Zellars, E. Boctor, and G. Hager, "Tracked regularized ultrasound elastography for targeting breast radiotherapy," *Medical Image Computing & Computer Assisted Interventions, MICCAI, London, UK*, pp. 507–515, Sept. 2009.
- [17] A. Lyschchik, T. Higashi, R. Asato, and et al., "Thyroid gland tumor diagnosis at US elastography," *Radiology*, vol. 237, no. 1, pp. 202–211, Aug. 2005.
- [18] F. Viola and W. Walker, "A comparison of the performance of time-delay estimators in medical ultrasound," *IEEE Trans. Ultrason. Ferroelectr. Freq. Control*, vol. 50, no. 4, pp. 392–401, Apr. 2003.
- [19] A. Pesavento, C. Perrey, M. Krueger, and H. Ermert, "A time efficient and accurate strain estimation concept for ultrasonic elastography using iterative phase zero estimation," *IEEE Trans. Ultrason. Ferroelectr. Freq. Control*, vol. 46, pp. 1057 – 1067, Sept. 1999.
- [20] H. Hasegawa and H. Kanai, "Improving accuracy in estimation of artery-wall displacement by referring to center frequency of rf echo," *IEEE Trans. Ultrason. Ferroelectr. Freq. Control*, vol. 53, no. 1, pp. 52–63, Jan. 2006.
- [21] J. Lindop, G. Treece, A. Gee, and R. Prager, "Phase-based ultrasonic deformation estimation," *IEEE Trans. Ultrason. Ferroelectr. Freq. Control*, vol. 55, no. 1, pp. 94–111, 2008.
- [22] W. Walker and G. Trahey, "A fundamental limit on delay estimation using partially correlated speckle signals," *IEEE Trans. Ultrason. Ferroelectr. Freq. Control*, vol. 42, no. 2, pp. 301–308, Mar. 1995.
- [23] F. Yeung, S. Levinson, and K. Parker, "Multilevel and motion model-based ultrasonic speckle tracking algorithms," *Ultrasound Med. Biol.*, vol. 24, pp. 427–441, Mar. 1998.
- [24] M. O'Donnell, R. Skovoroda, M. Shapo, and S. Emelianov, "Internal displacement and strain imaging using ultrasonic speckle tracking," *IEEE Trans. Ultrason. Ferroelectr. Freq. Control*, vol. 41, no. 3, pp. 314–325, Mar. 1994.
- [25] C. Sumi, "Usefulness of ultrasonic strain measurement-based shear modulus reconstruction for diagnosis and thermal treatment," *IEEE Trans. Ultrason. Ferroelectr. Freq. Control*, vol. 52, no. 10, pp. 1670 – 1689, Oct. 2005.
- [26] P. Barbone and J. Bamber, "Quantitative elasticity imaging: what can and cannot be inferred from strain images," *Phys. Med. Biol.*, vol. 47, pp. 2147–2164, Jun. 2002.
- [27] C. Sumi, "Reconstructions of shear modulus, poisson's ratio, and density using approximate mean normal stress lambda epsilon alpha alpha as unknown," *IEEE Trans. Ultrason. Ferroelectr. Freq. Control*, vol. 53, no. 12, pp. 2416 – 2434, Dec. 2006.
- [28] L. Bohs and G. Trahey, "A novel method for angle independent ultrasonic imaging of blood flow and tissue motion," *IEEE Trans. Ultrason. Ferroelectr. Freq. Control*, vol. 38, pp. 280–286, 1991.
- [29] P. Chaturvedi, M. Insana, and T. Hall, "2-d companding for noise reduction in strain imaging," *IEEE Trans. Ultrason. Ferroelectr. Freq. Control*, vol. 45, no. 1, pp. 179–191, Jan. 1998.
- [30] M. Rao, Q. Chen, H. Shi, T. Varghese, E. Madsen, J. Zagzebski, and T. Wilson, "Normal and shear strain estimation using beam steering on linear-array transducers," *Ultrasound Med. Biol.*, vol. 33, no. 1, pp. 57–66, Jan. 2007.
- [31] E. Konofagou and J. Ophir, "A new elastographic method for estimation and imaging of lateral displacements, lateral strains, corrected axial strains and poisson's ratios in tissues," *Ultrasound Med. and Biol.*, vol. 24, no. 8, pp. 1183–1199, 1998.
- [32] R. Maurice, J. Ohayon, Y. Fretigny, M. Bertrand, G. Soulez, and G. Cloutier, "Noninvasive vascular elastography: Theoretical framework," *IEEE Trans Med Imaging*, vol. 23, no. 2, pp. 164–180, Feb. 2004.
- [33] R. Maurice and M. Bertrand, "Lagrangian speckle model and tissue-motion estimation theory," *IEEE Trans Med Imaging*, vol. 18, no. 7, pp. 593–603, Feb. 1999.
- [34] M. Lubinski, S. Emelianov, K. Raghavan, A. Yagle, A. Skovoroda, and M. O'Donnell, "Lateral displacement estimation using tissue incompressibility," *IEEE Trans. Ultrason. Ferroelectr. Freq. Control*, vol. 43, no. 2, pp. 247–255, Mar. 1996.

- [35] C. Pellot-Barakat, F. Frouin, M. Insana, and A. Herment, "Ultrasound elastography based on multiscale estimations of regularized displacement fields," *IEEE Trans Med Imaging*, vol. 23, no. 2, pp. 153–163, Feb. 2004.
- [36] E. Brusseau, J. Kybic, J. Deprez, and O. Basset, "2-D locally regularized tissue strain estimation from radio-frequency ultrasound images: Theoretical developments and results on experimental data," *IEEE Trans Med Imaging*, vol. 27, no. 2, pp. 145–160, Feb. 2008.
- [37] C. Sumi, "Regularization of tissue shear modulus reconstruction using strain variance," *IEEE Trans. Ultrason. Ferroelectr. Freq. Control*, vol. 55, no. 2, pp. 297 – 307, Feb. 2008.
- [38] C. Sumi and K. Sato, "Regularization for ultrasonic measurements of tissue displacement vector and strain tensor," *IEEE Trans. Ultrason. Ferroelectr. Freq. Control*, vol. 55, no. 4, pp. 787 – 799, Apr. 2008.
- [39] G. Treece, J. Lindop, A. Gee, and R. Prager, "Uniform precision ultrasound strain imaging," *IEEE Trans. Ultrason. Ferroelectr. Freq. Control*, vol. 56, no. 11, pp. 2420–2436, 2009.
- [40] H. Rivaz, E. Boctor, P. Foroughi, G. Fichtinger, and G. Hager, "Ultrasound elastography: a dynamic programming approach," *IEEE Trans Med Imaging*, vol. 27, no. 10, pp. 1373–1377, Oct. 2008.
- [41] G. Welch and G. Bishop, "An introduction to the kalman filter," *University of North Carolina at Chapel Hill TR 95-041*, pp. 1–16, 1995.
- [42] A. Amini, T. Weymouth, and R. Jain, "Using dynamic programming for solving variational problems in vision," *IEEE Trans. Pattern Anal. Mach. Intell.*, vol. 12, no. 9, pp. 855–867, Sept. 1990.
- [43] P. Huber, *Robust statistics*. Wiley.
- [44] G. Hager and P. Belhumeur, "Efficient region tracking with parametric models of geometry and illumination," *IEEE Trans. Pattern Anal. Mach. Intell.*, vol. 20, no. 10, pp. 1025–1039, Oct. 1998.
- [45] P. Holland and R. Welsch, "Robust regression using iteratively reweighted least squares," *Commun. Statist. Theory Methods*, vol. A6, pp. 813–827, 1977.
- [46] L. Sandrin, M. Tanter, S. Catheline, and M. Fink, "Shear modulus imaging with 2-D transient elastography," *IEEE Trans. Ultrason. Ferroelectr. Freq. Control*, vol. 49, no. 4, pp. 426–435, Apr. 2002.
- [47] M. Tanter, J. Bercoff, L. Sandrin, and M. Fink, "Ultrafast compound imaging for 2-d motion vector estimation: application to transient elastography," *IEEE Trans. Ultrason. Ferroelectr. Freq. Control*, vol. 49, no. 10, pp. 1363–1374, Oct. 2002.
- [48] L. Chen, G. Treece, J. Lindop, A. Gee, and R. Prager, "A quality-guided displacement tracking algorithm for ultrasonic elasticity imaging," *Med. Imag. Anal.*, vol. 13, no. 2, pp. 286–296, Apr. 2009.
- [49] J. Prince and J. Links, *Medical imaging signals and systems*. Prentice Hall, 2006.
- [50] H. Shum and R. Szeliski, "Construction of panoramic mosaics with global and local alignment," *Internat. Journal Computer Vision*, vol. 36, no. 2, pp. 101–130, 2000.
- [51] S. Baker and I. Matthews, "Lucas-kanade 20 years on: A unifying framework," *Internat. Journal Computer Vision*, vol. 56, no. 3, p. 221–255, Feb. 2004.
- [52] R. Dugad and N. Ahuja, "Video denoising by combining kalman and wiener estimates," *Inter. Conf. Image Processing, ICIP*, vol. 4, pp. 152–156, 1999.
- [53] A. Jensen, "Field: A program for simulating ultrasound systems," *Medical & Biological Engineering & Computing*, vol. 34, pp. 351–353, 1996.
- [54] R. Wagner, S. Smith, J. Sandrik, and H. Lopez, "Statistics of Speckle in Ultrasound B-Scans," *IEEE Trans. Sonics and Ultrasonics*, vol. 17, no. 3, pp. 251–268, 1983.
- [55] H. Rivaz, E. Boctor, and G. Fichtinger, "Ultrasound speckle detection using low order moments," *IEEE Int. Ultrasonics Symp.*, pp. 2092–2095, Oct. 2006.
- [56] D. Bertsimas and J. Tsitsiklis, *Biomechanics: Mechanical Properties of Living Tissues*. Springer-Verlag, 1993.
- [57] T. Krouskop, T. Wheeler, F. Kallel, B. Garra, and T. Hall, "The elastic moduli of breast and prostate tissues under compression," *Ultras. Imag.*, vol. 20, pp. 260–274, 1998.
- [58] J. Liu, K. Abbey, and M. Insana, "Linear approach to axial resolution in elasticity imaging," *IEEE Trans. Ultrason. Ferroelectr. Freq. Control*, vol. 51, no. 6, pp. 716–725, Jun. 2004.
- [59] R. Padgett and C. Korte, "Assessment of the effects of pixel loss on image quality in direct digital radiography," *Physics Med. Biol.*, vol. 49, no. 6, p. 977–986, Mar. 2004.
- [60] M. Doyley, Q. Feng, J. Weaver, and K. Paulsen, "Performance analysis of steady-state harmonic elastography," *Physics Med. Biol.*, vol. 52, no. 10, pp. 2657–2674, May 2007.
- [61] X. Chen, M. Zohdy, S. Emelianov, and M. O'Donnell, "Lateral speckle tracking using synthetic lateral phase," *IEEE Trans. Ultrason. Ferroelectr. Freq. Control*, vol. 51, no. 5, pp. 540–550, May 2004.
- [62] E. Ebbini, "Phase-coupled two-dimensional speckle tracking algorithm," *IEEE Trans. Ultrason. Ferroelectr. Freq. Control*, vol. 53, no. 5, pp. 972–990, May 2006.
- [63] C. Sumi, "Displacement vector measurement using instantaneous ultrasound signal phase - multidimensional autocorrelation and doppler methods," *IEEE Trans. Ultrason. Ferroelectr. Freq. Control*, vol. 55, no. 1, pp. 24–43, Jan. 2008.
- [64] P. Foroughi, H. Rivaz, I. Fleming, G. Hager, and E. Boctor, "Tracked ultrasound elastography (true)," *Medical Image Computing & Computer Assisted Interventions, Beijing, China*, p. in press, Sept. 2010.
- [65] J. Jiang, T. Varghese, E. M. C. Brace, T. Hall, S. Bharat, M. Hobson, J. Zagzebski, and F. Lee, "Youngs modulus reconstruction for radio-frequency ablation electrode-induced displacement fields: A feasibility study," *IEEE Trans Med Imaging*, vol. 28, pp. 1325–1334, Aug. 2009.
- [66] J. Jiang, C. Brace, A. Andreano, R. DeWall, N. Rubert, T. Pavan, T. Fisher, T. Varghese, F. Lee, and T. Hall, "Ultrasound-based relative elastic modulus imaging for visualizing thermal ablation zones in a porcine model," *Phys. Med. Biol.*, vol. 55, pp. 2281–2306, 2010.
- [67] M. Miga, "A new approach to elastography using mutual information and finite elements," *Phys. Med. Biol.*, vol. 48, pp. 467–480, 2003.
- [68] M. Insana, L. Cook, M. Bilgen, P. Chaturvedi, and Y. Zhu, "Maximum-likelihood approach to strain imaging using ultrasound," *IEEE Trans. Ultrason. Ferroelectr. Freq. Control*, vol. 107, no. 3, pp. 1421–1434, 2000.